Nanoscale Horizons

ROYAL SOCIETY OF CHEMISTRY

REVIEW

View Article Online
View Journal | View Issue

Cite this: *Nanoscale Horiz.*, 2025, 10, 2262

From microchannels to high shear reactors: process intensification strategies for controlled nanomaterial synthesis†

Zixuan Feng,[a] Junheng Guo,*[a] Yingcheng Wang,[a] Jiaoyan Shi,[a] Huiwen Shi,[a] Haojie Li,[a] Jinli Zhang[ab] and Jiangjiexing Wu*[c]

Nanomaterials (NMs) have catalyzed transformative advancements across diverse technological domains owing to their exceptional size-dependent mechanical, optical, electronic, and chemical properties. However, the scalable and controllable synthesis of NMs remains a major challenge due to the complex interplay of nucleation and growth processes, which are highly sensitive to mixing, mass transfer, and heat transfer dynamics. In this context, process intensification (PI) strategies—originally developed in chemical engineering—have emerged as a powerful approach to overcome the inherent limitations of traditional batch synthesis. This review comprehensively analyzed seven representative PI reactors: microreactors, confined impinging jet reactors, rotating packed beds, high shear mixers, spinning disk reactors, ultrasonic reactors, and microwave reactors. We systematically examine their operating principles, enhancement mechanisms, advantages, and limitations in the context of NM synthesis. Furthermore, their applications in key areas such as biomedicine, adsorption, catalysis, coatings, optics, and electrochemistry are critically reviewed. Through comparative analysis and synthesis–structure–function correlation, this review aims to provide essential guidance for the rational selection and engineering of PI reactors toward controllable, sustainable, and high-throughput NM manufacturing, thereby advancing the frontiers of precision nanotechnology.

Received 13th May 2025,
Accepted 14th July 2025

DOI: 10.1039/d5nh00336a

rsc.li/nanoscale-horizons

1. Introduction

Nanotechnology is widely acknowledged as a critical enabling platform of the 21st century, driving both innovation and industrial transformation.[1] At the core of this technological revolution lie nanomaterials (NMs), typically defined as materials with at least one dimension ranging from 1 to 100 nm.[2,3] Due to their distinct small-size, quantum confinement, surface/interface, and macroscopic tunneling effects, NMs exhibit dramatically altered physicochemical properties compared to their bulk counterparts.[4] These unique characteristics underpin their extensive deployment in diverse fields such as textile functionalization,[5] environmental remediation,[6] smart agriculture,[7] bioengineering,[8] targeted therapeutics,[9] electronics,[10] and energy conversion and storage.[11] The global demand for high-performance NMs is growing rapidly, with production volumes surpassing 1.6 million metric tons in 2020[12] and market valuation projected to exceed $12.1 billion by 2026.[13] However, the synthesis of NMs with well-controlled size, morphology, composition, and surface chemistry remains a grand challenge. Conventional synthesis methods often involve hazardous chemicals, produce toxic by-products, lack

[a] School of Chemistry and Chemical Engineering/State Key Laboratory Incubation Base for Green Processing of Chemical Engineering, Shihezi University, Shihezi, 832003, China. E-mail: gjhtju@163.com
[b] School of Chemical Engineering and Technology, Tianjin University, Tianjin, 300072, China
[c] School of Marine Science and Technology, Tianjin University, Tianjin 300072, P. R. China. E-mail: wujiangjiexing2007@126.com, wjjx1987@tju.edu.cn

† Electronic supplementary information (ESI) available. See DOI: https://doi.org/10.1039/d5nh00336a

Zixuan Feng

Zixuan Feng is currently pursuing her MS degree at the School of Chemical Engineering and Technology, Shihezi University under the supervision of Associate Professor Junheng Guo. She received her BS degree from Shihezi University in 2024. Her research interests are the micromixing performance of high shear mixers and the preparation of nanomaterials.

control over size distribution, exhibit low efficiency, show batch-to-batch inconsistency, consume high energy, and raise environmental concerns. Therefore, the development of innovative preparation technologies and advanced manufacturing strategies that integrate green chemistry principles and sustainable intensification is crucial for maximizing the potential of NMs and addressing the growing demand for high-performance NMs in both fundamental research and industrial applications.[14]

Process intensification (PI), as a transformative concept in chemical engineering, emphasizes the integration of advanced process designs and high-efficiency equipment to significantly enhance mass transfer, heat transfer, and momentum transfer efficiencies.[15] Simultaneously, it improves the safety and productivity of manufacturing processes, thereby achieving substantial reductions in processing costs, energy consumption, and waste emissions in chemical processes.[16] In recent years, a variety of PI technologies and devices have been developed with the aim of achieving precise control over molecular mixing, mass transfer, and heat transfer. These include microreactors, confined impinging jet reactors, rotating packed beds, high shear mixers, spinning disk reactors, ultrasonic reactors, and microwave reactors, all of which have garnered significant attention (Scheme 1). Such devices enable the overcoming of traditional kinetic and thermodynamic equilibrium limitations, leading to higher reaction yields and more consistent product quality in chemical reactions and material synthesis.[17] The role of PI strategies in the nanoparticles (NPs) formation process is shown in Fig. 1(A).[18] It can be concluded that the development of PI technology and its associated equipment provides an innovative pathway for the efficient and controllable synthesis of NMs. In addition, based on the publication statistics from the Web of Science database (Fig. 1(B)), since 2004, research on the aforementioned reactors for NMs synthesis has demonstrated a rapid upward trend. Further word cloud analysis (Fig. 1(C)) indicates that studies in this area predominantly concentrate on biomedicine, electrochemistry, catalysis, adsorption, optics, and coatings. This highlights the significant practical demand within these fields and reflects the strong interest of researchers in advancing NMs synthesis technologies.

From left to right: Junheng Guo and Haojie Li

Junheng Guo is an Associate Professor at Shihezi University. He received his PhD degree in 2023 from Tianjin University under the supervision of Professor Jinli Zhang. His research focuses on process intensification techniques (such as high shear mixer) and their application in the synthesis of functional nanomaterials.
Haojie Li is an Associate Professor at Shihezi University. He received his PhD degree in 2022 from Tianjin University under the supervision of Professor Jinli Zhang. His research focuses on process intensification techniques (such as microreactor) and their application in the field of heat transfer.

From left to right: Jiaoyan Shi, Yingcheng Wang, and Huiwen Shi

Yingcheng Wang is currently pursuing his MS degree at the School of Chemical Engineering and Technology, Shihezi University under the supervision of Associate Professor Junheng Guo. He received his BS degree from Zhengzhou University of Light Industry in 2023. His research interest is the application of high shear mixers in non Newtonian fluids.
Jiaoyan Shi is currently pursuing her MS degree at the School of Chemical Engineering and Technology, Shihezi University under the supervision of Associate Professor Junheng Guo. She received her BS degree from Qujing Normal University in 2024. Her research interest is the application of process intensification equipment in organic synthesis.
Huiwen Shi is currently pursuing his MS degree at the School of Chemical Engineering and Technology, Shihezi University under the supervision of Associate Professor Junheng Guo. He received his BS degree from Yantai University in 2024. His research interest is the application of high shear mixers in strengthening low melting point solvents.

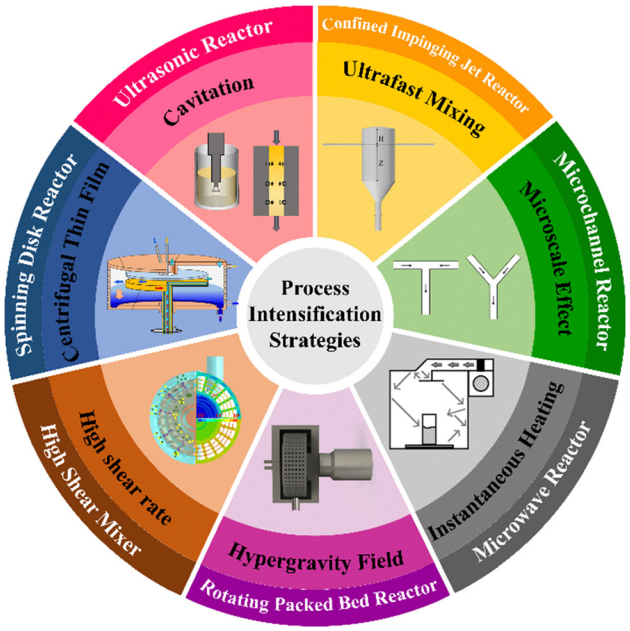

Scheme 1 Classification and main features of PI equipment.

Despite the growing interest, there remains a lack of comprehensive reviews that summarize the mechanistic insights, reactor performance characteristics, and application-specific outcomes of PI strategies in NM synthesis. To fill this gap, this review provides a systematic overview of seven representative PI reactors, highlighting their role in modulating nucleation, growth, and functionalization pathways of NMs. Moreover, we summarize emerging research trends and interdisciplinary applications, offering a robust theoretical basis and practical guidance for reactor selection and design to meet diverse performance requirements in nanotechnology-driven fields. Consequently, this will not only facilitate the optimization of NMs synthesis pathways but also enhance interdisciplinary collaboration and accelerate the development of sustainable and high-throughput manufacturing processes.

2. Types and characteristics of PI technologies

2.1 Microchannel reactor

The core structure of a microchannel reactor (MCR) is composed of a network of microchannels with dimensions smaller than 1 mm. The micrometer-scale characteristic size enables it to surpass the physical transfer limitations of conventional reactors, conferring advantages such as a high specific surface area,[19] rapid response time,[20] narrow residence time distribution,[21] superior heat and mass transfer properties,[22,23] efficient mixing capabilities, and inherent safety.[24] Consequently, MCR are widely employed in chemical reactions and the synthesis of NMs, among other processes.[25] To meet diverse application scenarios and requirements, MCR can be customized and optimized to achieve various fluid contact configurations. Typically, MCR can be designed in forms such as continuous flow and Taylor flow (Fig. 2(A)).[26]

Continuous flow MCR predominantly exhibit single-phase flow characteristics. Common reactor designs include T-shaped, Y-shaped and cross-shaped configurations. Among these, the cross-shaped MCR elucidates the formation mechanism of NPs (Fig. 2(B)).[27] In continuous flow MCR, NPs demonstrate high supersaturation levels, short nucleation induction times, and uniform spatial distribution, facilitating the production of particles with small sizes and narrow size distributions.[28] Furthermore, the precise control of process parameters in MCR allows for fine-tuning of the size, morphology, composition, and structure of NPs, ensuring high selectivity, low energy consumption, and excellent reproducibility of the reaction. Additionally, continuous flow MCR can operate effectively across a wide range of flow rates and solvent types. However, the deposition of precursors and/or products on the channel walls may induce fouling, which can compromise flow dynamics, accelerate reactor aging, and potentially lead to blockage.[29]

In contrast, Taylor flow MCR are predominantly gas–liquid and liquid–liquid multiphase systems. Typically, an immiscible fluid is introduced into the channel to partition the reaction

Jinli Zhang

Jinli Zhang is a Professor at Tianjin University. He is a fellow of the Institution of Chemical Engineers (FIChemE). His research focuses on process intensification technologies (e.g., high shear mixers, microreactors) and their applications in the green chemistry industry.

Jiangjiexing Wu

Jiangjiexing Wu, an Associate Professor at Tianjin University, primarily focuses on the intensified preparation and application of functional nanomaterials (such as nanozymes). Congratulations to Nanoscale Horizons on a decade at the forefront of nanoscience! Our journey began in 2018 with a publication that received the Outstanding Paper Award, marking a significant milestone in our research. It was a further privilege to join the Community Board and contribute to this vibrant scientific community. We are thrilled to celebrate this anniversary with a perspective highlighting process intensification strategies in nanomaterial synthesis. Congratulations to Nanoscale Horizons—wishing continued success in the years ahead.

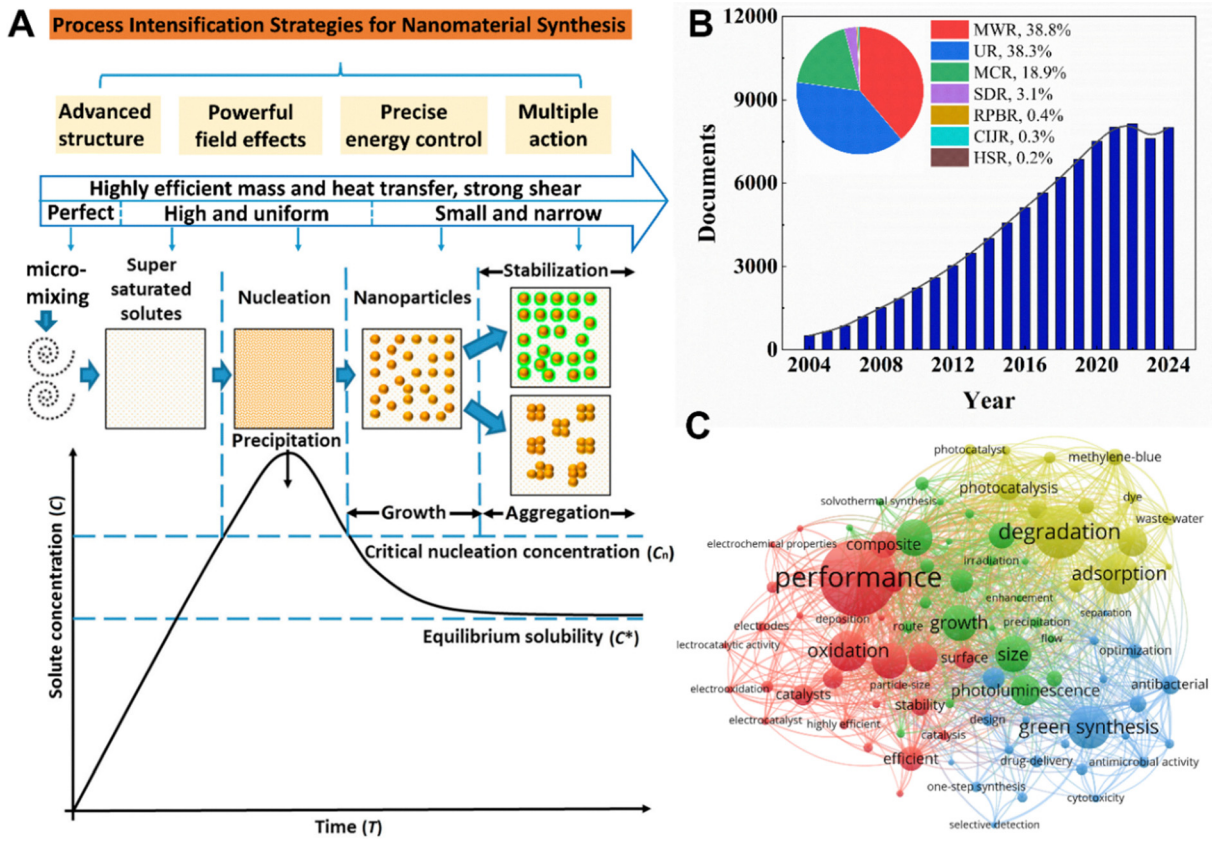

Fig. 1 (A) La Mer model and Schematic diagram of the role of PI strategies in the formation of NPs. (B) Document publications over the years. (C) Keyword cloud map. Reprinted with permission from ref. 18. Copyright 2019 Elsevier.[18]

mixture into a series of discrete "plugs" or "droplets", thereby generating Taylor flow. This approach facilitates self-recycling enhanced mixing, effectively reducing axial dispersion and narrowing the residence time distribution.[30–32] Droplet-based microfluidic technology employs isolated droplets as MCR, which not only increases the interfacial area but also enhances mixing and mass transfer rates through internal recycling and symmetric vortices that induce fluid folding and stretching. The encapsulation provided by the second phase in Taylor flow protects NPs from contacting the microchannel walls, thereby minimizing fouling, preventing undesirable channel blockage or contamination, and extending the lifespan of the reactor.[33,34]

Moreover, MCR can be synergistically optimized by integrating them with external fields such as acoustic, electric, gravitational, pressure fields, or stirring mechanisms. This integration aims to enhance their intrinsic performance or broaden their application scope. From an industrialization perspective, MCR can adopt the "numbering-up" strategy, enabling parallel operation for scaling up production.[35] This approach not only avoids the performance degradation typically associated with traditional scale-up methods but also provides a feasible pathway for the small-batch continuous production of high-value-added NMs and chemicals.[36,37]

2.2 Confined impinging jet reactor

The core structure of the confined impinging jet reactor (CIJR) comprises a micro-mixing chamber with symmetric nozzles. Generally, the chamber diameter is at least twice that of the impinging jet inlet (Fig. 3(A)).[38] A high-pressure pump drives two axially opposed linear jets to collide at high velocities (1–100 m s^{-1}). The instability of the impinging flow results in the conversion of kinetic energy into turbulent motion through a redirection of flow. High-frequency velocity pulsations within localized turbulent vortices induce periodic oscillations, thereby establishing a high-energy dissipation zone (Fig. 3(B)).[39] As a result, materials are uniformly mixed, and a uniform supersaturated environment for reactants is achieved within an extremely short time frame (on the millisecond level), markedly enhancing the local mass transfer rate and reaction rate (Fig. 3(C)).[39–43] Consequently, the CIJR does not necessitate external mechanical energy for promoting mixing, mass transfer, or heat transfer; it is widely applied in the synthesis of NPs *via* flash nano-precipitation (FNP).[44,45]

The formation process of NPs in the CIJR is analogous to that in the MCR. Both micro-mixing and macro-mixing times are comparable, reaching the millisecond level, which is several orders of magnitude shorter than those in traditional stirred tank reactor (STR).[46] However, the CIJR's susceptibility to blockage due to its small channel dimensions and lack of external mechanical forces limits its suitability for handling systems with high solid content or high viscosity. Despite this limitation, compared to conventional stirred tanks, the CIJR features a simpler structure, higher fluid turbulent energy

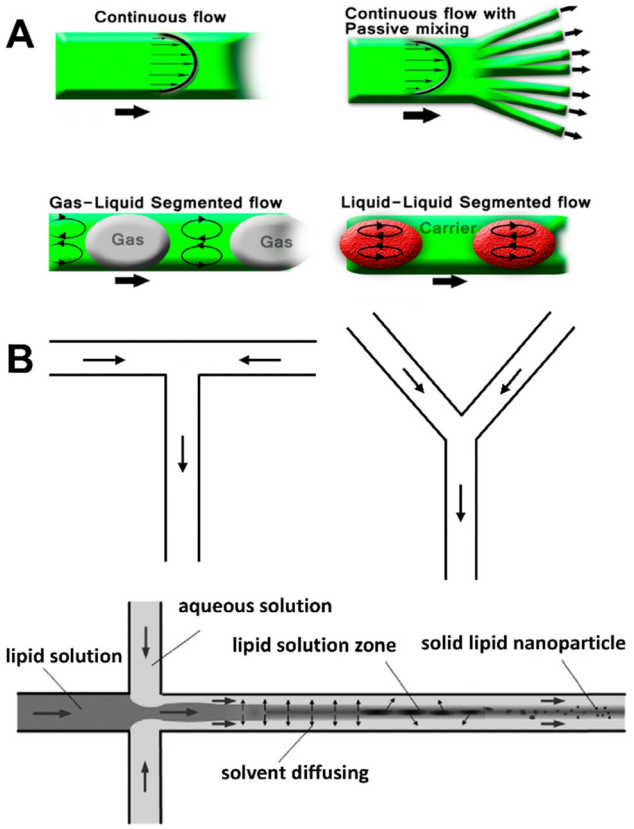

Fig. 2 (A) Comparison of different MCR flow systems. Reprinted with permission from ref. 26. Copyright 2016 IntechOpen.[26] (B) T-shaped, Y-shaped and cross-shaped MCRs. Adapted with permission from ref. 27. Copyright 2017 Elsevier.[27]

dissipation rates, and reduced power input requirements, providing advantages in terms of resistance to blockage and prevention of NPs agglomeration. In the CIJR, as the Reynolds number increases, the thickness of the impingement zone decreases while local kinetic energy and energy dissipation rates increase correspondingly. Consequently, the liquid jet flow rate, as an important process parameter, significantly influences the fluid kinetic energy and pressure fluctuations within the impingement zone, thereby determining the energy and mass transfer characteristics of the solution in the CIJR and the mixing efficiency of the microjets.[47,48] Additionally, the compact design of the CIJR enables it to achieve high production NPs synthesis applications.[49]

2.3 Rotating packed bed reactor

The rotating packed bed reactor (RPBR), also known as the high gravity reactor, is a highly efficient device for PI. It utilizes a rotor rotating at ultrahigh speeds ($\sim 10^3$ rpm) to generate an intense centrifugal force field ($\sim 10^2$ g).[52–54] As depicted in Fig. 4(A), the core structure of an RPBR typically comprises three main components: a high-speed rotor packed with specialized fillers, a stationary outer casing, and a liquid distributor. During operation, fluids are introduced into the internal packing zone through one or more fixed distributors. Under the influence of the ultrahigh centrifugal force field, the liquid is forced to flow radially outward. The rapidly rotating packing materials continuously fragment the liquid into micron-scale thin films, liquid ligaments, or droplets along the packing trajectory (Fig. 4(B)).[50,54,55] This process dramatically enhances the gas–liquid or liquid–liquid interfacial contact area while significantly reducing the thickness of the mass transfer boundary layer. Consequently, RPBR achieves remarkable improvement in molecular mixing and diffusion processes *via* these intensified mechanisms.[56–58]

The RPBR enables uniform mixing of reactants within milliseconds, achieving a highly uniform supersaturation distribution. Its characteristic micromixing time (10^{-4}–10^{-5} s) is significantly shorter than the nucleation induction time of most NPs in aqueous solutions ($\sim$1 ms), thereby fulfilling the requirement for ideal homogeneous nucleation where micromixing precedes induction.[59–61] Furthermore, the uniformly mixed solution within the RPB is subjected to ultrahigh centrifugal forces, causing it to fragment into micron-scale droplets, liquid films, and ligaments upon collision with porous packing materials. Rapid nucleation of NPs occurs within these confined units (Fig. 4(C)).[51] The nucleation process rapidly

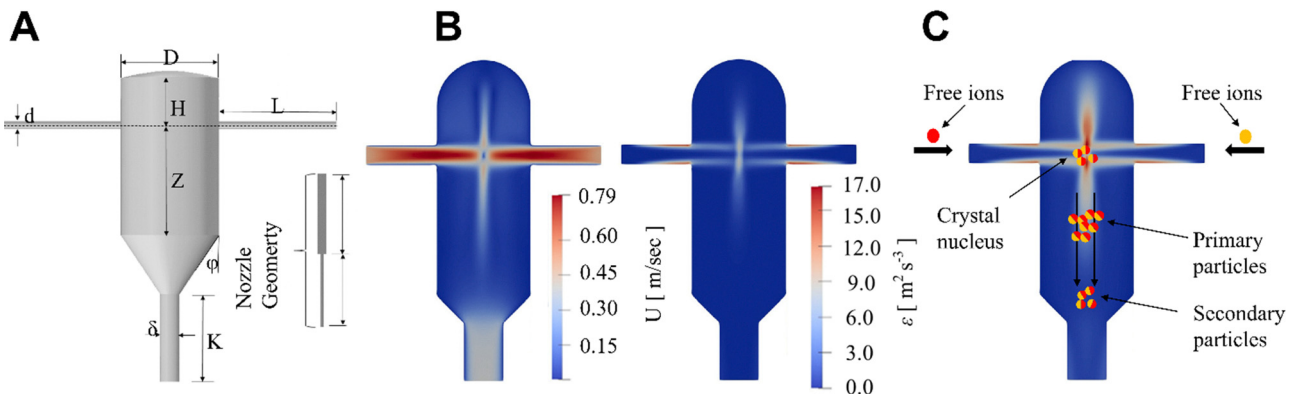

Fig. 3 (A) Schematic diagrams of the CIJR and the nozzle. Reprinted with permission from ref. 38. Copyright 2021 Elsevier.[38] (B) The magnitude of the velocity and turbulence dissipation rate contour plots. (C) Formation process of NPs in CIJR. Reprinted with permission from ref. 39. Copyright 2023 Elsevier.[39]

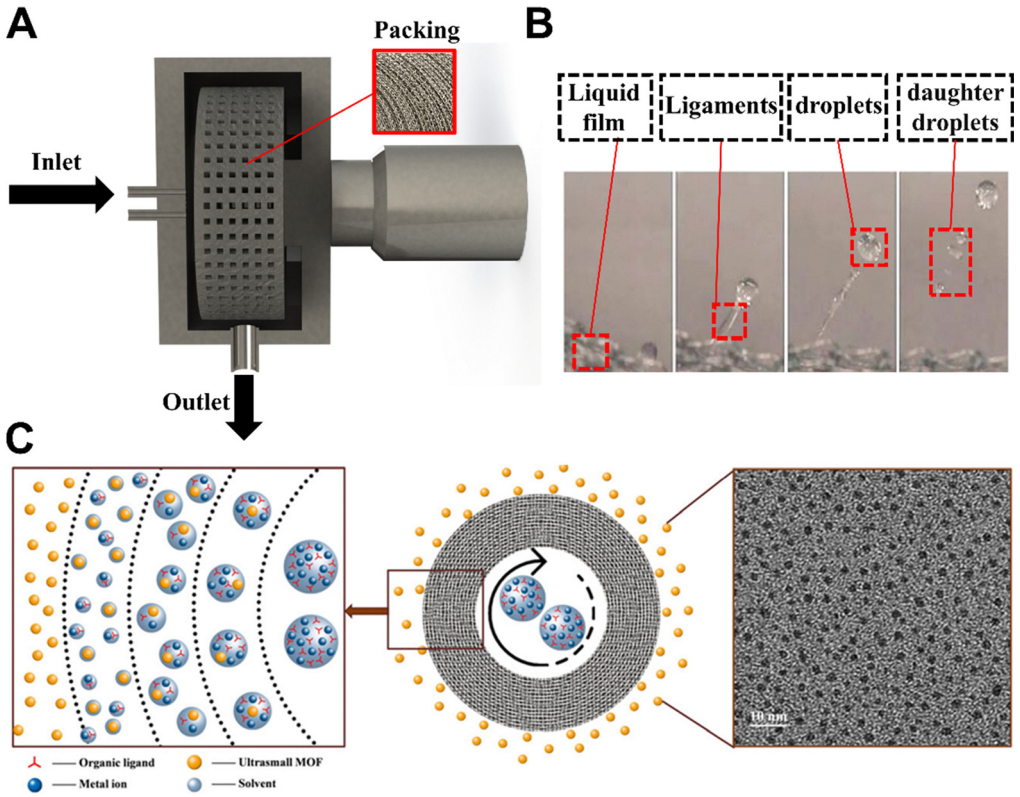

Fig. 4 (A) Schematic diagram of the RPBR setup. (B) Evolution of liquid flow patterns in the RPBR. Reprinted with permission from ref. 50. Copyright 2017 Elsevier.[50] (C) Schematic illustration of ultrasmall MOF formation. Adapted with permission from ref. 51. Copyright 2021 Wiley-VCH.[51]

depletes reactants within these units, effectively restricting post-nucleation growth and providing favorable conditions for the synthesis of small-sized NPs.[62,63]

Additionally, the short residence time (<1 s) in the RPB limits secondary growth of formed particles and prevents Ostwald ripening (where larger particles consume smaller ones), ensuring particle uniformity.[64] By fine-tuning operational parameters such as rotational speed and flow rate ratio, the nucleation, growth, and size distribution of NPs can be precisely controlled, enabling the targeted synthesis of high-quality NMs with high production efficiency.[65] However, prolonged operation may result in wear of packing materials caused by rigid NPs, clogging due to adhesive NPs under high solid content, and reduced dispersion efficiency for high-viscosity liquids within dense packing structures, which partially constrains the application of RPBs in NM synthesis processes.

2.4 High shear mixer

The high shear mixer (HSM), also referred to as the high shear reactor (HSR) or rotor–stator mixer, incorporates a core component—the high-shear mixing head—comprising a high-speed rotor ($\sim 10^4$ rpm) and a stationary stator. The synergistic interaction between the rotor and stator induces intense mechanical shear, ultrahigh shear rates ($\sim 10^6$ s^{-1}), and energy dissipation rates ($\sim 10^6$ m^2 s^{-3}). These forces facilitate rapid deformation, dispersion, and fragmentation of fluid microclusters, emulsion droplets, bubbles, and particle aggregates. This mechanism enables PI in crystal morphology control,[67,68] emulsification,[69–71] dispersion and mass transfer,[72–74] deagglomeration,[75,76] mixing,[77–79] and chemical reactions (Fig. 5(A) and (B)).[66,80,81] Owing to these capabilities, HSM has been widely utilized across various domains, including chemical engineering, pharmaceuticals, cosmetics, energy, and advanced materials.[82,83] HSM demonstrates superior performance in single-phase, gas–liquid, liquid–liquid, and gas–liquid–solid systems, as well as in fluids with viscosities ranging from 0.1 cP to 10^5 cP.[83] Its mass transfer and micromixing efficiencies surpass those of conventional stirred-tank reactors by 1–2 orders of magnitude, while its volumetric footprint can be reduced to 1/10–1/5 of traditional equipment at equivalent throughput, providing substantial advantages for industrial-scale production.[68] Notably, HSM's exceptional anti-clogging capability renders it particularly suitable for high solid-content systems, establishing it as an ideal tool for large-scale controlled synthesis of NMs.[66]

Typically, the particle size of NPs leaving the reactor is determined by the interplay of nucleation, growth, coalescence, agglomeration, and fragmentation processes (Fig. 5(C)).[66] Similar to RPB, HSMs exhibit a characteristic micromixing time ($\sim 10^{-4}$ s), enabling precise control over nucleation and growth processes to produce NPs with small sizes and narrow size distributions. Distinctively, the intense shear forces in HSMs play critical roles in suppressing particle coalescence, breaking agglomerates,[75] modulating secondary nucleation, controlling crystal facet growth,[67] and tailoring crystal morphology,[68] providing novel

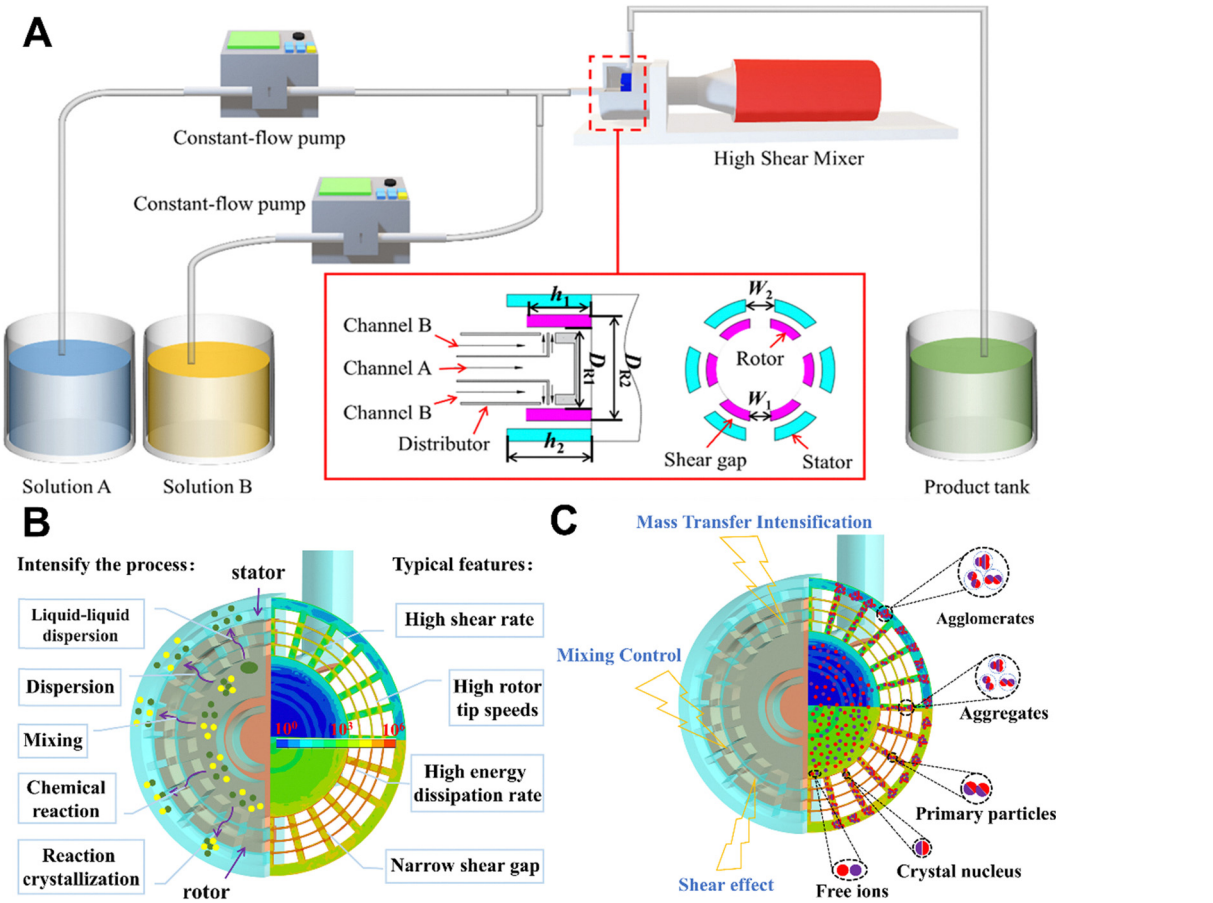

Fig. 5 (A) Schematic diagram of the HSR experimental setup. (B) Key characteristics and application scope of the HSR. (C) Preparation process of NPs in the HSR. Reprinted with permission from ref. 66. Copyright 2025 American Chemical Society.[66]

strategies for NM synthesis. Furthermore, HSMs can operate in both batch and continuous modes, with adjustable residence times ranging from short durations (1–10^2 s) to extended periods (10^2–10^4 s),[76,84] ensuring adaptability to diverse operating conditions and process stages (*e.g.*, synthesis and maturation). The ability of HSMs to generate uniform micro/nanoemulsions within minutes further enhances their utility for emulsion synthesis.[71] By fine-tuning operational parameters such as rotor speed, feed flow rate, and geometric features of the rotor–stator assembly and distributors, HSMs allow precise regulation of micromixing time,[78] shear intensity,[79] residence time,[85] and ultimately NPs size and morphology,[67] facilitating large-scale controlled NMs production. However, the challenge of fluid back-mixing-induced secondary growth in HSM systems remains a key consideration in NM synthesis.

2.5 Spinning disk reactor

The Spinning disk reactor (SDR) is characterized by its core component—a disk capable of rotating at high speeds (up to 10^3 rpm). During the operation of the SDR, the fresh material jet is introduced into the injection zone on the surface of the rotating disc through the liquid-phase inlet(s) located at the top of the disc (Fig. 6(A)).[86–88] Under the influence of centrifugal force, the material spreads radially outward, transitioning from the acceleration region to the synchronous region while gradually attaining a velocity nearly equivalent to the rotational speed of the disc. Consequently, this process facilitates the formation of a thin, highly sheared film with a thickness ranging between 20 and 300 micrometers (Fig. 6(B)).[89] First, the liquid film provides short diffusion and conduction path lengths. Second, high rotational speeds enhance surface wave intensity and induce high-intensity turbulence within the liquid membrane. This shearing effect generates numerous waves and ripples in the membrane, thereby promoting lateral mixing across its thickness.[90,91] Moreover, the SDR achieves a more uniform velocity distribution at any given radial location, minimizing radial dispersion and exhibiting hydrodynamic properties that closely resemble piston flow.[92] Concurrently, the rapid flow over the disk's surface leads to a significantly reduced residence time.

The thinner liquid film and strong turbulence within the liquid film of the SDR not only enhance heat and mass transfer as well as reaction rates but also enable a microscopic mixing time (~1 ms) comparable to that of the aforementioned reactors.[93] This provides a significant advantage in facilitating rapid chemical reactions, such as polymerization, crystallization, and competitive fast chemical reactions, as well as in the preparation of NMs.[94,95] The disc rotation speed, the nature

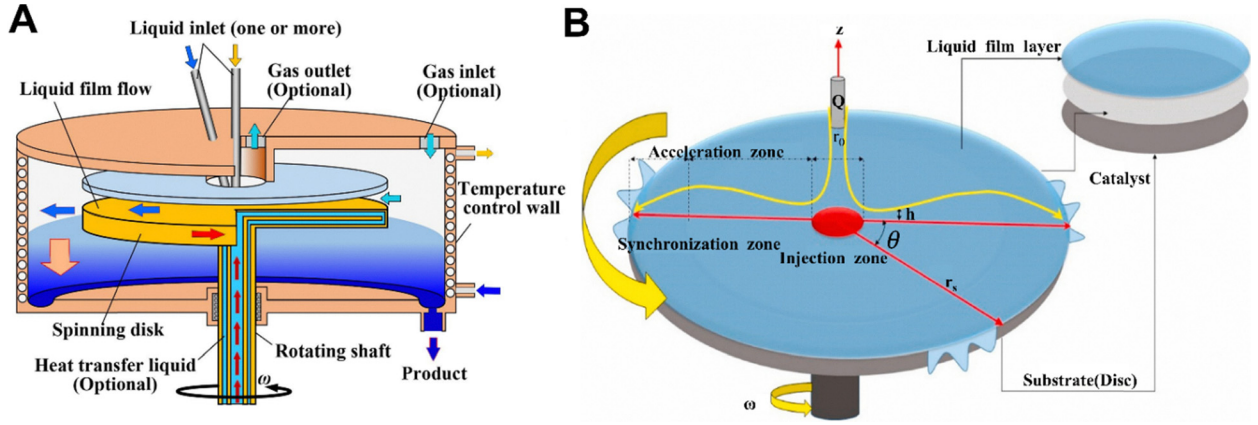

Fig. 6 (A) Schematic diagram of the basic components and operating principle of the SDR. Adapted with permission from ref. 88. Copyright 2023 Elsevier.[88] (B) Location of the injection, acceleration and synchronization zones on the disk. Adapted with permission from ref. 89. Copyright 2024 Elsevier.[89]

of the disc surface (smooth or grooved), the flow rate of the reaction stream, and the position of the inlet stream feed collectively influence micromixing efficiency, residence time distribution, and consequently particle characteristics.[96,97] Nitrogen or other inert gases are frequently utilized to displace oxygen within the reactor, effectively inhibiting undesired chemical reactions.[98]

Compared to the conventional STR, the SDR shows superior safety performance.[99] Additionally, in contrast to RPBR and HSM, the SDR exhibits flow characteristics that more closely approximate plug flow, which not only significantly increases the frequency of particle collisions but also effectively reduces particle agglomeration.[99–101] Furthermore, SDR requires significantly lower pumping energy, while demonstrating some resistance to fouling or clogging, which underscores its potential for large-scale commercialization.[86,101,102] However, the substantial degradation of mixing and mass transfer performance at elevated material viscosity remains a critical issue that cannot be overlooked. Additionally, the short residence time limits its applicability in particle size regulation and the preparation of larger-sized NMs.

2.6 Ultrasonic reactor

The ultrasonic reactor (UR) employs ultrasonic radiation to induce cavitation effects, thereby intensifying fluid mixing, dispersion, and mass transfer processes. Specifically, high-frequency acoustic waves (20 kHz–10 MHz) prompt the rapid formation, growth, and collapse of numerous microbubbles within microseconds (Fig. 7(B)).[103–105] This process generates intense shear forces, turbulent flows, liquid circulation, micromixing, and free radicals.[106] Collectively, these mechanisms enhance mixing efficiency, accelerate mass transfer rates, and improve chemical reaction kinetics. The cavitation effect restricts the growth of nucleation centers formed during bubble generation due to the extremely short cavity collapse time. This not only shortens reaction times but also ensures rapid contact and interaction of reactant molecules, significantly increasing nucleation rates. Consequently, URs provide favourable conditions for synthesizing NPs with higher crystallinity, smaller particle sizes, and narrower size distributions.[107–109]

Furthermore, cavitation induces extreme localized conditions within microseconds, including transient high temperatures (~5000 K), pressures (~1000 bar), and ultra-high heating/cooling rates (~10^{10} K s^{-1}).[110,111] These conditions establish unique physicochemical environments for NMs synthesis and modification, effectively reducing activation energies, accelerating reaction kinetics, and enabling reactions that are otherwise difficult to achieve under conventional conditions.[112] Ultrasonically synthesized particles often exhibit porous structures and high surface areas,[113–115] which enhance

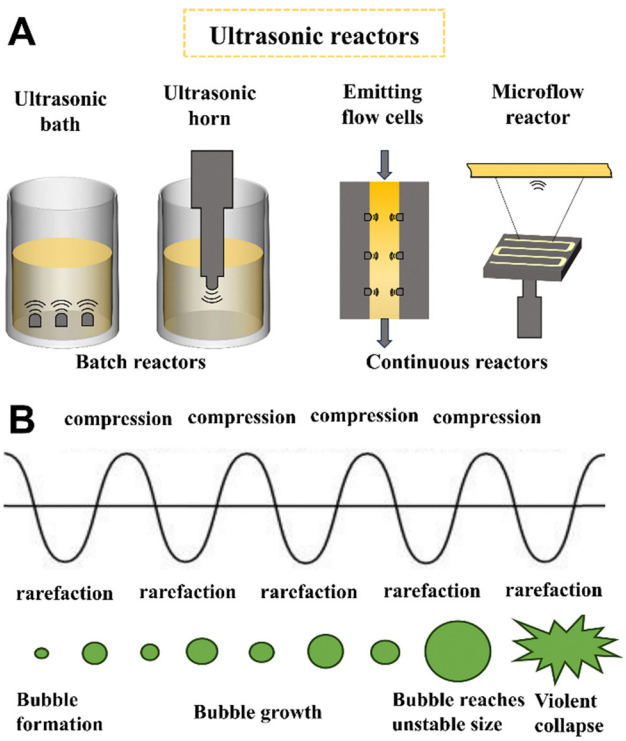

Fig. 7 (A) Types of UR and corresponding equipment for each category. (B) Formation of microbubbles. Adapted with permission from ref. 121. Copyright 2024 Elsevier.[121]

their catalytic activity in various applications.[116,117] Additionally, the mechanical effects of cavitation break up particle aggregates and dislodge particles adhered to channel walls. By precisely adjusting ultrasonic frequency, power, and exposure time, the morphology, size distribution, and properties of materials can be finely controlled.[118–120] Ultrasonic reactors are classified into batch systems (*e.g.*, ultrasonic baths and submersible probes) and continuous configurations (Fig. 7(A)).[121] Batch reactors are primarily utilized in laboratory-scale studies, while continuous systems are better suited for large-scale industrial production. However, batch reactors face limitations due to uneven acoustic field distribution and challenges in scalability, which restrict their broader industrial adoption.

2.7 Microwave reactor

Conventional heating typically only heats the outer surface of the heated object and relies on conduction or convection for heat transfer. However, the microwave Reactor (MWR) employs microwave radiation to convert electromagnetic energy into thermal energy, which is directly transferred to the heated object *via* interaction with microwaves, without affecting the surrounding environment. Microwave radiation can penetrate materials, thereby generating heat uniformly throughout the material and achieving more efficient and uniform heat transfer.[122,123] Fig. 8(A) illustrates the difference in heating mechanisms between conventional and microwave heating.[124] MWR can be divided into two types: single-mode and multimode reactors. Single-mode reactors irradiate a single vessel, providing a highly uniform energy field that enables rapid and precise heating. In contrast, multimode reactors are equipped with larger cavities capable of accommodating multiple vessels simultaneously. These reactors often require stirrers or other mechanisms to enhance the uniformity of the electromagnetic field distribution within the solvent (Fig. 8(B)).[125]

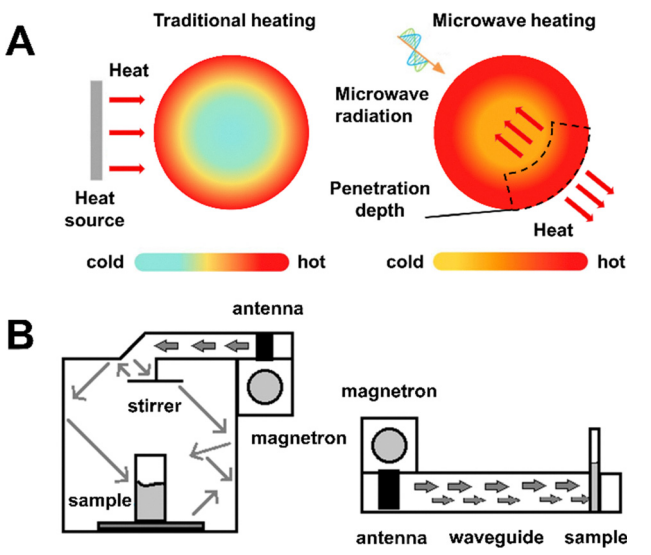

Fig. 8 (A) Different heating models for conventional and microwave heating. Reprinted with permission from ref. 124. Copyright 2025 Royal Society of Chemistry.[124] (B) Multimode system and single-mode cavity. Adapted with permission from ref. 125. Copyright 2012 Springer Nature.[125]

Microwave radiation demonstrates reduced energy requirements, characterized by its high penetration depth and the ability to achieve rapid temperature modulation. This facilitates challenging chemical reactions under mild conditions while providing precise control over reaction dynamics, thereby enhancing nucleation and chemical reaction rates by several orders of magnitude.[126–128] Microwave radiation can also reduce the deposition of NPs on the reactor wall.[129,130] Selective heating is accomplished through the exploitation of specific ions' microwave energy absorption capabilities and the "hot spot" effect,[131,132] leading to high selectivity and fine-tuned control over crystal morphology for achieving a uniform particle size distribution.[133,134] Microwave technology can drastically reduce reaction times from days to minutes,[135] even in dry medium conditions, minimize solvent consumption and by-product formation,[136,137] and improve product quality, yield, and reproducibility, thus enabling the green and efficient synthesis of NMs.[137–140] However, the limited microwave penetration depth constrains its applicability in large-volume reactors. The integration of microwave heating with continuous flow technology represents a promising strategy to overcome this limitation.

For the convenience of readers' understanding, the comparison table of abbreviations and their full names mentioned in this review can be found in Table S1 of the ESI.† In the previous content, we elaborated in detail on the superiority of the PI device, and in Table S2 (ESI†), we compared the micromixing performance (such as micromixing time and local turbulent kinetic energy dissipation rate) among the reactors and the particle size of the NMs materials obtained. Although these technologies have been widely adopted, their maturity and economic competitiveness remain major obstacles to further development compared with traditional methods. The limitations and problems that still exist in current PI technologies are listed in Table S3 (ESI†).

3. Advanced applications of PI-fabricated NMs

In advancing NM performance, PI technologies and equipment serve as indispensable enablers by inducing multi-dimensional structural reconfigurations in materials through the application of finely controlled physical and chemical fields. These include: precise control over particle size to surpass the threshold of quantum size effects, fabrication of gradient porous architectures to maximize surface area and mass transfer efficiency, directional grafting of surface functional groups to engineer highly active interfaces, and simultaneous regulation of lattice defects while increasing the density of active sites. Importantly, PI systems exhibit strong synergistic effect in the concurrent optimization of compositional, morphological, and interfacial properties. By precisely managing crystallization kinetics, PI techniques not only facilitate the formation of

highly monodisperse nanocrystalline clusters but also construct heterostructures with tuneable crystal face exposure. Moreover, dynamic charge-balancing mechanisms enable the regulation of atomic-scale surface charge distribution, further enhancing electrochemical uniformity and functional stability. This multi-dimensional, cross-scale modification strategy not only elevates the intrinsic physicochemical properties of NMs, but also establishes a rational design pathway by mapping structural features directly to performance metrics. As a result, PI-fabricated NMs unlock their full potential in high-value fields such as biomedicine, catalysis, optics, energy systems, and other frontier technologies. Below, we discussed the representative applications. The contributions of the PI equipment in the preparation of these NMs are presented in the ESI† in the form of Table S4. Meanwhile, Table S5 (ESI†) compares the traditional methods with the PI device. It provides specific data on reaction time, material size, specific surface area, pore size and pore volume, productivity and yield, as well as application performance, to more intuitively demonstrate the outstanding performance of the PI devices.

3.1 Application in the biomedical field

Biomaterials span a wide array of forms and functions, including gels, pharmaceuticals, and additives, each demanding tailored NM properties. In gel systems, the synthesis of nanoprecursors with small particle sizes and narrow size distributions is crucial to achieving uniform crosslinking and robust mechanical integrity. Simultaneously, mild fluid dynamics and low shear stress are essential to prevent structural degradation during synthesis. The characteristics of MCR and CIJR, particularly their narrow residence time distribution and minimal shear forces, render them highly suitable for the preparation of such precursors. A cascaded CIJ microreactor system enables the efficient synthesis of hydroalcoholic gel hand sanitizers (GHS) containing carboxymethyl chitosan/Zn(II)/proanthocyanidins antimicrobial NPs.[141] This method effectively minimizes alcohol evaporation, enhances product quality, and extends shelf life. Hands treated with GHS demonstrated significant microbial reduction after 12 hours. Moreover, high-pressure CIJR restricts the growth of microgel precursors, resulting in smaller particle sizes and narrower size distributions.[142] This facilitates uniform crosslinking, yielding highly stable stimuli-responsive poly(*N*-vinylcaprolactam) gels while avoiding issues associated with surfactant residues and cytotoxicity.

For non-gel systems, reactors with intense turbulence and shear effects, such as SDR, RPBR, and HSR, play essential roles in nanopharmaceutical and additive manufacturing. Small particle sizes and narrow size distributions are critical for ensuring rapid dissolution and product stability. RPBR enables the controlled preparation of monodisperse spherical $CaCO_3$ NPs with an average size of approximately 6 nm, achieving reduced energy consumption alongside mass transfer rates enhanced by 1–2 orders of magnitude and a 56% improvement in productivity.[143] As highly stable (>18 months) super-alkaline nano-additives, the integration of these materials into lubricating oils significantly extends the service life of modern machinery. In the biomedical field, drug absorption depends largely on dissolution kinetics. Poorly water-soluble drugs have limited dissolution rates in the gastrointestinal tract, reducing bioavailability. Drug nanocrystals increase the specific surface area to enhance dissolution and improve bioavailability. Additionally, amorphous irbesartan NPs prepared *via* RPBR exhibit approximately 13.5-fold higher saturation solubility than raw drugs within 10 min and achieve 100% *in vitro* dissolution within 30 min, maintaining amorphous stability for over 6 months of storage.[144] SDR further enhances the continuous synthesis of nimesulide NPs with smaller sizes and narrower distributions through liquid antisolvent precipitation, reducing the complete dissolution time from 180 to 80 min while significantly improving dissolution. rates and bioavailability.[145] These reactors demonstrate remarkable advantages in scalable, efficient, and controllable production of non-gel nanobiomaterials.

Encapsulation and coating are extensively employed in nanobiomaterial synthesis. NPs can serve as drug delivery platforms and biological imaging probes. These systems can efficiently enhance tissue compatibility, and increase cellular uptake efficiency, achieving precise delivery. Therefore, optimizing the design of nanocarriers to encapsulate hydrophobic drugs and unstable bioactive substances is a key strategy for improving bioavailability and diagnostic accuracy. UR excel in structural modulation by altering local microenvironments. For instance, UR facilitates the ethanol-free self-assembly of zein and sodium caseinate into stable spherical NPs (225.94 nm ± 3.84 nm).[146] Under ultrasonic assistance, these NPs efficiently encapsulate hydrophobic curcumin, forming smooth, dense surfaces that enhance stability and sustain release—achieving 78.4% retention at 95 °C and 86.91% ± 0.72% DPPH radical scavenging capacity. Coupling UR with MCR enables continuous clog-free production of fragile mRNA lipid NPs with 98.3% mRNA encapsulation efficiency, maintaining stable and potent luciferase expression 24 hours post-injection of a 10 μg dose in mice.[147] Notably, PLA/DDAB NPs were continuously synthesized at a throughput of 1.6 g h^{-1} for 1.5 h without clogging (Fig. 9). The integration of high shear technology with cavitation effects in the hydrodynamic cavitation reactor (HCR) facilitates the formation of stable oil-in-water nanoemulsions (366.4 nm, PDI 0.298), which enhance nicotinamide release (4335.8 μg cm^{-2} cumulative release at 12 h) and penetration while reducing pore occlusion in skincare applications.[148] These synergistic integrations of non-contact energy input technologies (UR, MWR) with PI equipment (MCR, HSR) not only overcome traditional reactor limitations such as clogging and narrow applicability but also achieve superior synthesis outcomes, establishing a versatile platform for advanced biomaterial fabrication.

3.2 Application in the adsorption field

Enhancing specific surface area, optimizing pore structure, exposing more active sites, reducing agglomeration, and improving dispersion are not only critical strategies for improving the performance of adsorption materials but also represent the core advantages and objectives of process-intensified reactors in regulating the synthesis of nano-adsorbents. For example, the confined jet impingement-continuous microchannel

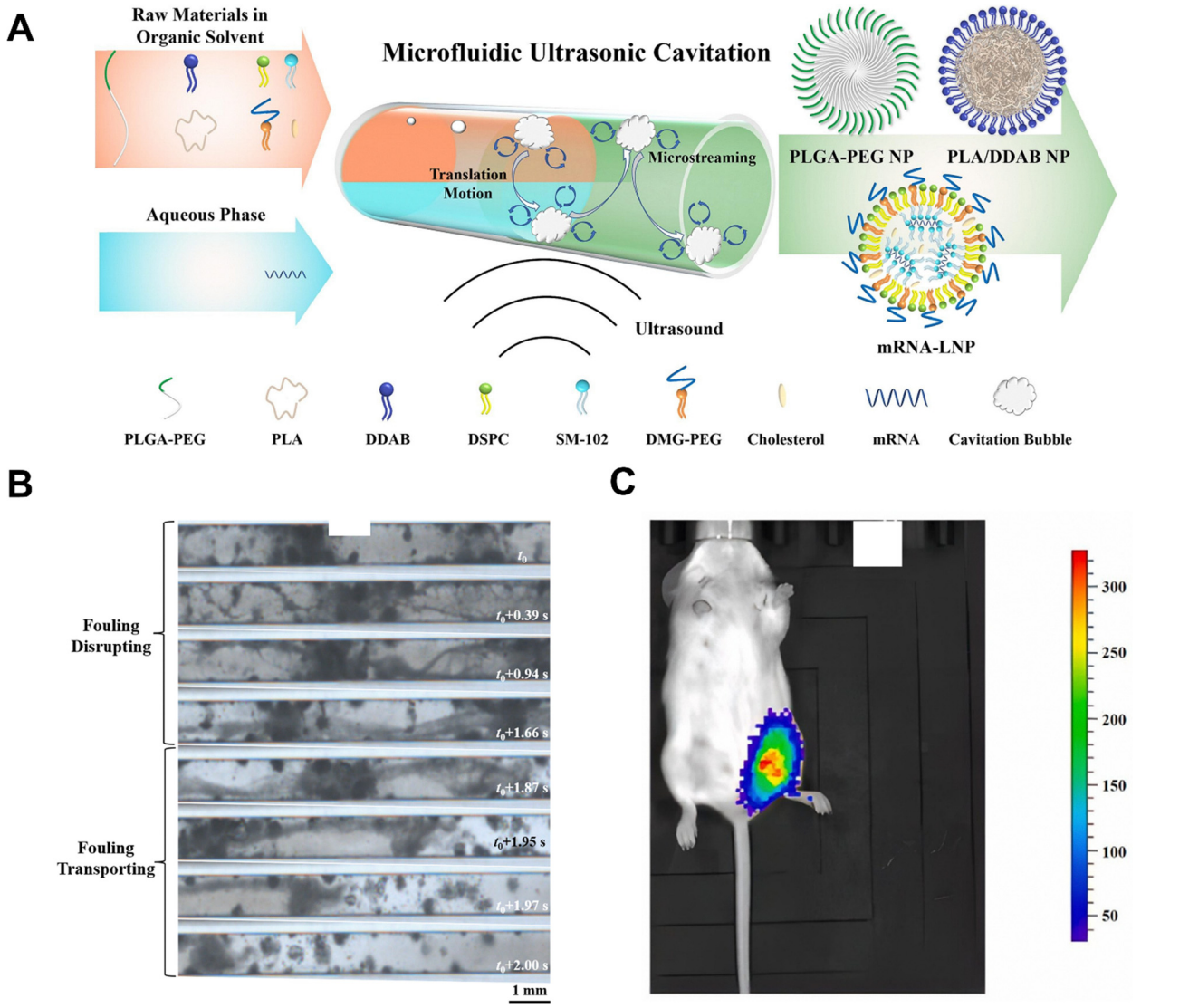

Fig. 9 (A) Schematic illustration of microfluidic ultrasonic cavitation approach for synthesis biomedical organic NPs. (B) The fouling detaching process by ultrasonic cavitation in the microchannel. (C) *In vivo* bioluminescence imaging of reporter mRNA-LNP synthesized by microfluidic ultrasonic cavitation approach in mice. Adapted with permission from ref. 147. Copyright 2023 Elsevier.[147]

reactor (CJI-CMR) demonstrates exceptional capabilities in increasing specific surface area.[149] It enables the preparation of mesoporous silica NPs (MSNs) with ultra-high specific surface areas ranging from 1347 to 1854 $m^2\ g^{-1}$ and lightweight worm-like mesoporous structures. When used as a silicon source, the resulting Li_4SiO_4 achieves a CO_2 adsorption capacity of 27.18 wt% at 650 °C, with only a 1.1 wt% decline after 10 adsorption/desorption cycles. Zr-based metal–organic frameworks (Zr-MOFs) were reduced to the nanoscale using an internal circulation rotating packed bed (ICRPB).[150] Defects and stacking interactions increased pore volume, promoting water cluster formation and improving pore-filling efficiency. Compared to micron-scale Zr-MOFs made with a traditional STR, the ICRPB process achieved 26.5% yield in 1 minute, with a 50% faster reaction rate. The resulting product adsorbed water vapor at 625 mg g^{-1}, with the adsorption rate increasing 2.0–2.8 times (Fig. 10). Global industrialization and chemical use have increased pollutant levels, including heavy metals, antibiotics, and dyes, in aquatic ecosystems. Functionalizing nanoadsorbents with biomolecules, carbon materials, or polymers improves pollutant separation, adsorption capacity, and recyclability. Similarly, the IS-RPB system, which integrates CIJR and RPB, exhibits outstanding performance in preparing carboxymethyl cellulose-stabilized nano zero-valent iron and effectively reduces NP agglomeration and increases active sites, achieving a maximum Pb^{2+} adsorption capacity of 1237.32 mg g^{-1}.[151]

PI reactors enhance NM dispersion through two primary pathways: improving raw material dispersion and optimizing NP distribution. The high turbulence and shear forces generated within the RPB significantly improve the dispersion of hydrous ferric oxide (HFO) NPs in D201 resin, yielding

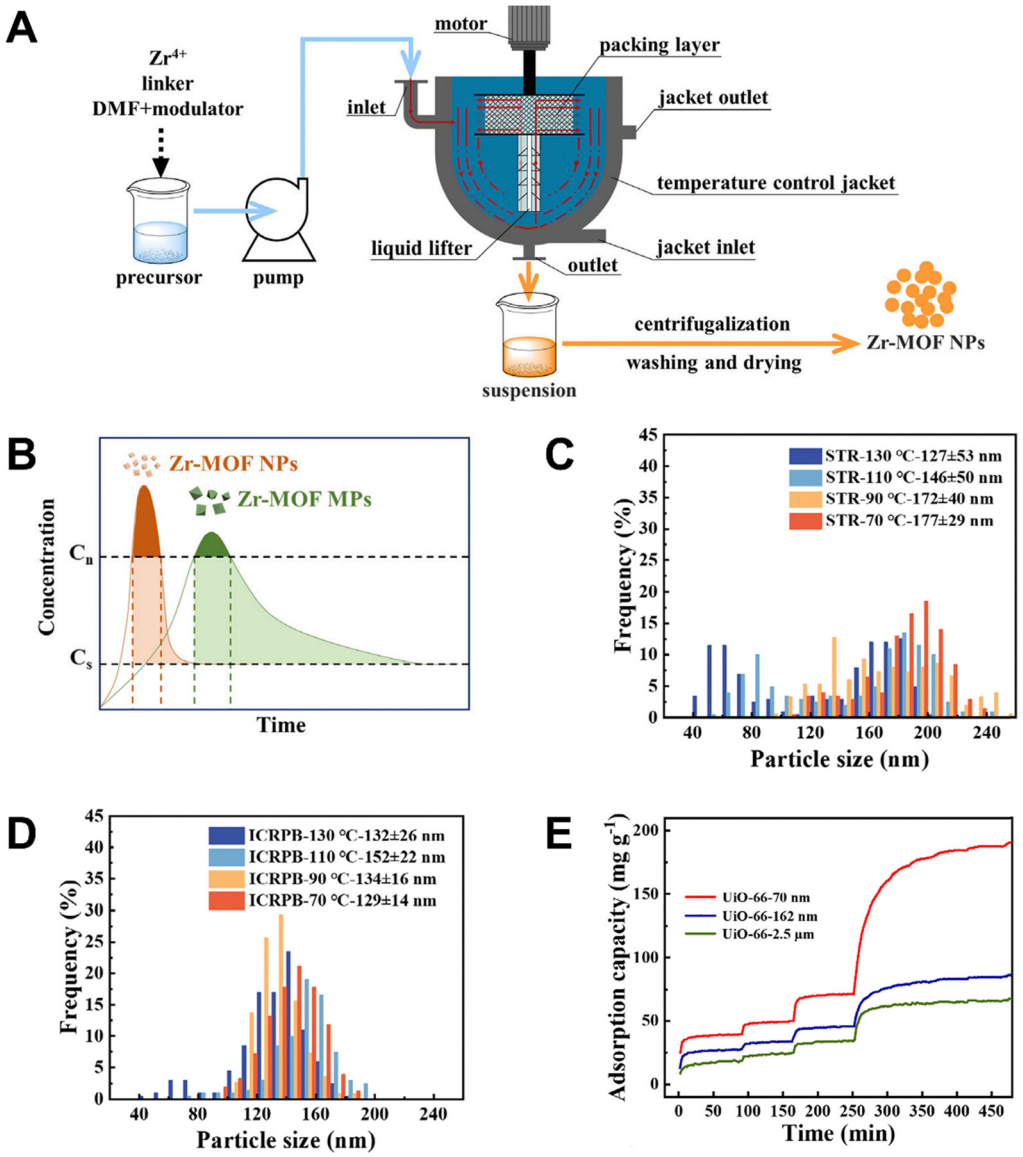

Fig. 10 (A) The synthetic route in ICRPB. (B) Schematic illustration of Zr-MOF nucleation and growth according to the LaMer mode. The particle size distributions of Zr-MOF were synthesized at a rotating speed of 500 rpm with (C) STR, (D) ICRPB. (E) Water adsorption capacity–time curves. Adapted with permission from ref. 150. Copyright 2023 John Wiley and Sons.[150]

D201-HFO nanocomposites (D201-HFO-R) with small average particle size, narrow size distribution, and elevated specific surface area.[152] These composites achieve a Cr(VI) removal efficiency of 99.7% while reducing reaction time to one-fifth of conventional methods. MWR excel in NM dispersion control, as demonstrated by microwave-assisted synthesis of CeO_2 NPs uniformly dispersed on highly crystalline multi-walled carbon nanotubes (MWCNTs).[153] The resulting 9% CeO_2/MWCNTs composite shows enhanced surface hydroxyl groups, achieving an adsorption capacity of 62.1 mg g^{-1} and a removal rate of 95.3% for methylene blue (MB).

Energy shortages and environmental degradation are driving the global community to seek clean energy solutions, among which nuclear energy and hydrogen energy are expected to play a key role in future energy systems. However, how to achieve efficient uranium capture and solve the problems of hydrogen transportation and storage remains a key challenge that requires innovative solutions. For pore structure optimization, HSR-induced nanobubbles enable the functionalization of hierarchical silica mesoporous microspheres (HSMSMs) with amidoxime (AO) groups, creating HSMSMs-AO with high surface area, large pore volume, short parallel channels, and rapid adsorption equilibrium.[154] This material demonstrates exceptional uranium adsorption capacity (607 mg g^{-1}) with high selectivity in multi-ion environments. The combination of microwave-assisted and microfluidic technology enables *in situ* heating, overcoming the thermal conductivity limitations of conventional methods. This approach facilitates the one-step synthesis of Cu-BDC@rGO composites with significantly reduced processing time.[155] The sandwich-structured

composite, featuring MOFs encapsulating reduced graphene oxide (rGO) sheets, shows an 18% higher yield and a 26% enhanced hydrogen adsorption capacity (77 K, 40 bar) compared to conventional methods. Air pollutants and greenhouse gases emitted from the combustion of fossil fuels and industrial production will have adverse effects on the environment and human health. The control and remediation of air pollution through nano-adsorbents is regarded as an advanced treatment technology. Additionally, microwave-assisted reverse micelle synthesis produces Th^{4+}-based MOF NMs composed of spherical nanorod clusters (~20 nm), exhibiting enhanced pore size, surface area, and thermal stability.[156] Compared with the same materials prepared by the ultrasonic-assisted method, these materials have higher adsorption capacities for CO and CH_4 at room temperature.

Meanwhile, the large-channel design of HSR minimizes clogging risks, making them suitable for complex multiphase systems. For instance, achieving near-complete conversion of $Ca(OH)_2$ to stable calcite with HCl outlet concentrations below 30 mg m^{-3}. HSR enables counter current contact of HCl/CO_2 with carbide slag slurry, This process simultaneously achieves pollutant capture and green resource utilization of industrial waste.[157]

3.3 Application in the catalysis field

The catalytic efficiency of nanocrystals exhibits a significant structure–activity relationship with their surface morphology characteristics, wherein the atomic arrangement pattern of the exposed crystal faces on the periphery plays a critical role. PI equipment exerts a decisive influence on the performance optimization of synthesized nano-catalytic materials, primarily in three aspects: First, it significantly optimizes the surface defect density through precise control of lattice distortion. Second, it effectively increases the distribution density and accessibility of active sites, including acidic centers and oxygen vacancies. Most importantly, it establishes efficient charge transfer pathways, facilitating the directional migration of electrons, reactants, and products. This synergistic effect ultimately leads to the formation of an advantageous catalyst system characterized by high surface energy states and open mesoporous structures, which not only markedly improves reaction conversion rates and selectivity but also effectively suppresses side reactions and reduces reaction cycle times.

High-gravity fields or ultrasonic technology enable precise particle size control, reducing agglomeration and improving uniformity of surface area, pore volume, and elemental distribution. Based on these methodologies, a highly catalytically active Cu–Mn composite oxide catalyst ($Cu–MnO_x/\gamma$-Al_2O_3) was successfully synthesized within 45 minutes using the RPBR-assisted impregnation method, achieving a total organic carbon removal rate of up to 93.4% within 20 min.[158] Moreover, the MnO_2/SnO_2 nano-catalyst system prepared *via* the UR-assisted co-precipitation method exhibited a catalytic efficiency of 84.4% for H_2O_2 decomposition.[159]

HSR can enhance the density of surface acidic sites on nanocatalysts, promote the formation of oxygen vacancies, and increase the proportion of active species. These synergistic effects significantly improve the overall catalytic performance, thereby enhancing raw material conversion rates, target product selectivity, and product yield. Traditional co-precipitation methods rely on surfactants or solvents, raising environmental and economic concerns. In contrast, high shear-assisted technology converts $CsCu_{0.1}H_{2.9}PMo_{11}VO_{40}$ from irregular bulk structures into uniform particles without additives, enhancing porosity and surface smoothness.[161] Applied to methyl acrolein conversion to methyl acrylic acid, this catalyst achieved 83.4% conversion and 87.1% selectivity. For two-dimensional NMs, MnAl mixed metal oxides (MnAl-MMOs) typically exhibit dense packing due to layer spacing constraints. High shear force exfoliates these materials into ordered structures with expanded gaps,[162] exposing active sites.[163] This modification improves NO conversion and N_2 selectivity in NH_3 catalytic reduction to 96.3% and 91%, respectively. Compared to high-shear mixing technology, ultrasonic cavitation further reduces the diameter of bimetallic NiMo nanocatalysts without significantly altering their metal ratios, thereby enhancing the quality and stability of synthetic oil during vacuum residue upgrading.[164]

Waste from the textile and pharmaceutical industries often contains toxic and biologically refractory organic pollutants. Photocatalytic technology is renowned for its economic feasibility and environmental sustainability. It degrades organic pollutants by absorbing solar energy, reducing pollution in aquatic ecosystems. Microwave thermal effects increase nitrogen doping in carbon quantum dots (CQDs) and control morphology, regulating electronic structure and spectral bands.[165] A hybrid semiconductor (N-CQDs) formed in 1 minute degraded rose red dye by 93%. The SDR-assisted sol–gel method synthesizes small TiO_2 particles without solvents, enabling copper doping and phase transformation.[166] This approach reduces bandgap energy, increasing formic acid generation in CO_2 reduction by 15–21%. SDR assistance boosts Ag NPs production to 0.49 g h^{-1}, enabling uniform embedding in zeolite carriers.[167] The resulting AgNP-Z catalyst degrades MB by 74% under visible light within 6 hours. The customization of BiOX nanocatalysts ($BiOCl_xBr_{1-x}$) with varying halogen doping ratios was achieved using four-stream multi-inlet vortex mixer (MIVM)-assisted FNP technology.[160] The resulting $BiOCl_xBr_{1-x}$ had a uniform petal-like morphology and a bandgap energy of 2.89 eV, balancing light absorption and oxidation capacity. During tetracycline (TC) photocatalytic degradation, the rate constant was 5 times higher than traditional methods, achieving over 90% TC removal after 40-min visible light irradiation (Fig. 11).

3.4 Application in the coating field

In general, the application of NMs in coatings can be categorized into three types based on coating preparation processes: (1) simultaneous synthesis of NMs and coating solutions followed by application; (2) *in situ* formation of coatings on substrates during NM synthesis, primarily utilized for textiles; (3) sequential preparation of NMs prior to coating fabrication.

For the first category, reactors must exhibit robust shear and dispersion capabilities to simultaneously regulate NM

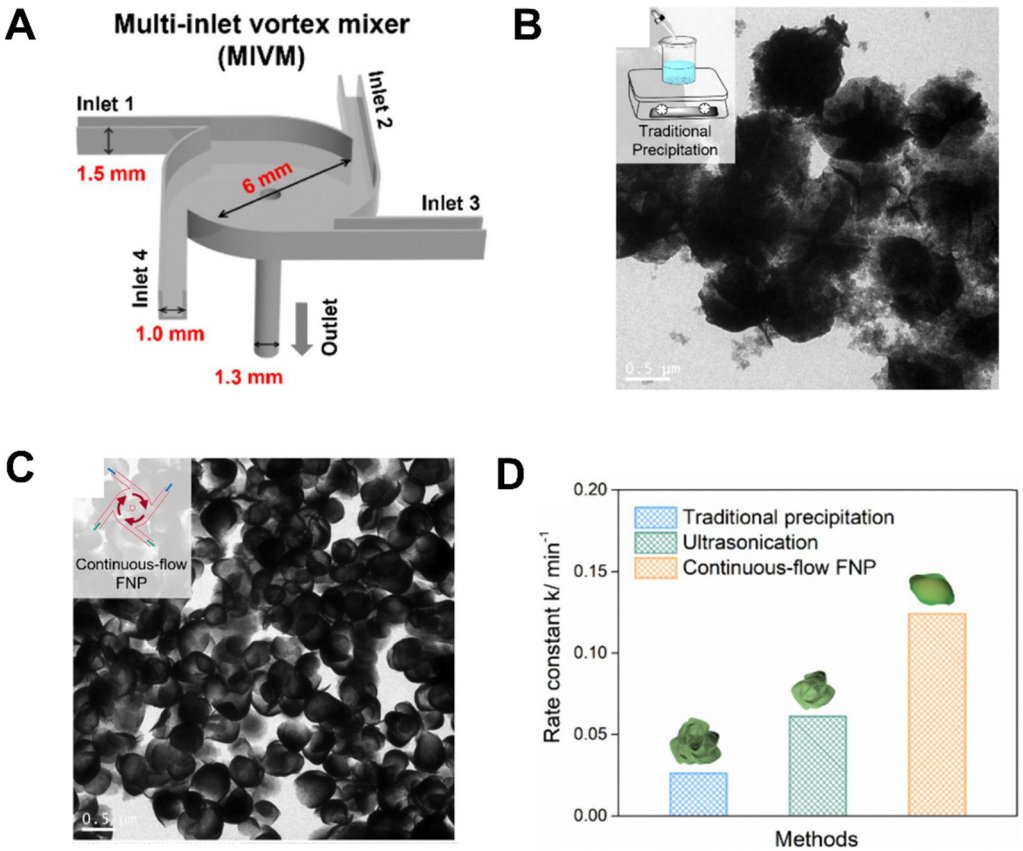

Fig. 11 (A) Diagram of the four-stream MIVM. Morphological comparation of $BiOCl_{0.75}Br_{0.25}$ samples processed by (B) traditional nanoprecipitation, (C) FNP. (D) Comparation of kinetic rate constants of the $BiOCl_{0.75}Br_{0.25}$ photocatalysts processed by different methods for TC degradation. Adapted with permission from ref. 160. Copyright 2024 Elsevier.[160]

synthesis and enhance dispersion efficiency. The combination of UR and HSR proves highly effective, significantly reducing mixing time.[168] This approach not only intercalates polymer chains into layered silicate clay interlayers but also achieves uniform clay dispersion in polyurethane (PU) coatings. Consequently, PU composite coatings containing 3 wt% clay demonstrate a 34.4% improvement in adhesive strength, with contact angles reduced to 56.66° and corrosion rates decreased to 0.0002 mm per year.

The second category benefits from non-contact PI technologies such as UR and MWR, whereas reactors with moving components (RPBR, HSR, SDR) pose risks of substrate damage. In recent years, antibacterial noble metals (*e.g.*, Ag) and transition metal oxides (*e.g.*, ZnO, TiO_2) NMs have played a key role in the textile industry by inducing bacterial cell wall or membrane rupture *via* surface lattice defects or specific free radicals. These materials are widely used in developing multifunctional smart textiles. For instance, ultrasonic cavitation avoids thermal degradation of textiles while promoting TiO_2 crystallization, Ag^+ reduction, and Fe_3O_4 formation, enabling one-step *in situ* synthesis of core–shell structured TiO_2:Fe_3O_4:Ag nanocomposites.[169] This method enhances NM adsorption and uniform distribution on polyester fabrics. Ultrasound-assisted emulsification further facilitates the preparation of vitamin E-encapsulated spherical NPs using bovine serum albumin and silk fibroin carriers.[170] Cotton fabrics coated with these NPs exhibit negligible cytotoxicity, strong antioxidant activity, sweat-resistant stability, and accelerated degradation in 95% ethanol with approximately 40% vitamin E release within 48 hours. Ultrasonic treatment induced glycosidic bond cleavage in cellulose while preserving fabric integrity, generating mechanical free radicals that reduced metal ions (Ag^+, Au^{3+}) *in situ*.[171] This promoted uniform dispersion of Ag and Au NPs in the cellulose matrix, enabling preparation of environmentally friendly cellulose-based nanocomposites with antibacterial and catalytic properties. This method avoids toxic reagents and simplifies the process compared to conventional techniques (Fig. 12). Microwave radiation decomposes trisodium citrate into dihydroxyacetone, releasing electrons to reduce Ag^+ to Ag^0.[172] Spherical Ag-NPs synthesized *in situ* are evenly dispersed on cotton fibers. These NPs absorb UV radiation *via* localized surface plasmon resonance above 120 °C, providing UPF 50+ protection. Cotton fibers with smaller NPs (which increase the contact area with bacterial surfaces) and higher NP loading exhibit enhanced antibacterial activity and UV shielding.

For the third category, the coupling of HSR with hydrothermal methods excels in enhancing NP crystallinity. This method successfully synthesized highly crystalline, antibacterial spherical ZnO NPs, which can function as an efficient film coating to effectively inhibit the enzymatic browning of avocados.[173] UR-assisted precipitation improves crystallinity, AgI/TiO_2

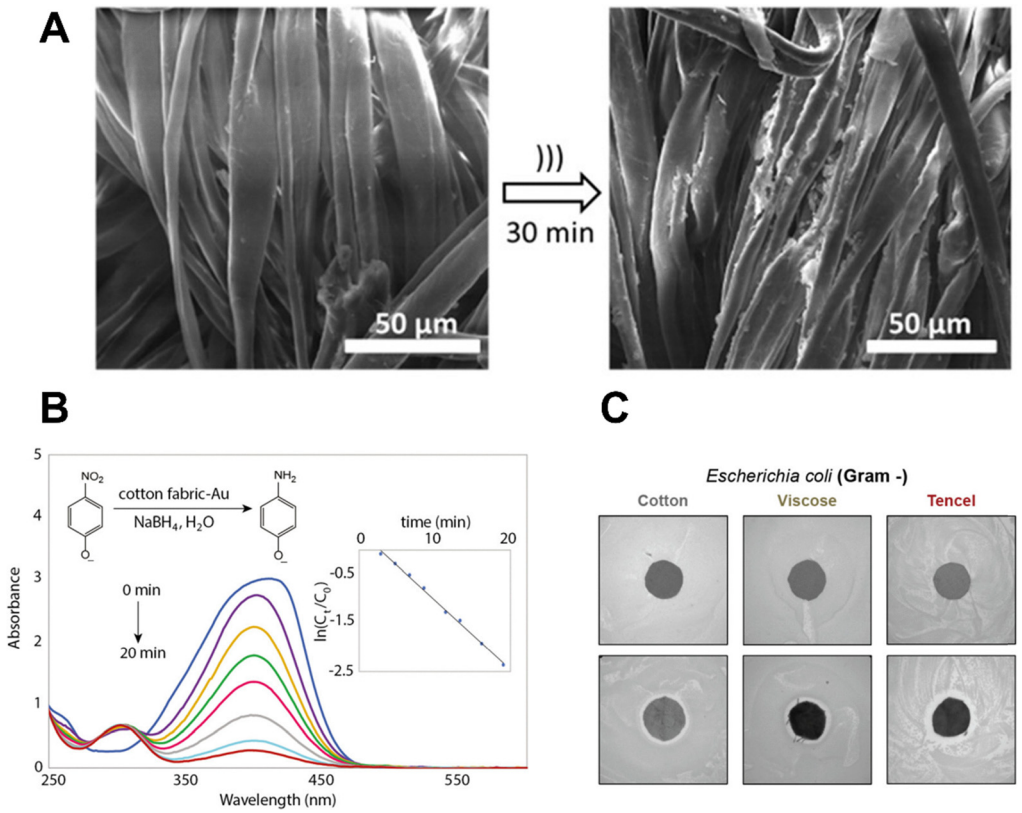

Fig. 12 (A) SEM images of the cotton fabric before (left) and after 30 min of sonication (right). (B) 4-NPh reduction catalyzed by the cotton fabric–Au nanocomposite followed by UV-vis spectroscopy. The reaction follows first-order kinetics as shown by the linear $\ln(C_t/C_0)$ *vs.* time plot (inset). (C) Area of inhibition of fabrics on agar growing *Escherichia coli*. Adapted with permission from ref. 171. Copyright 2020 American Chemical Society.[171]

nanocomposites exhibit a blue-shifted visible light absorption band (430 → 424 nm).[174] Corrosion of engineering materials threatens infrastructure and manufacturing. Nano-coatings reduce porosity and fill defects to prevent the penetration of harmful environmental factors, improving long-term corrosion resistance and extending service life. UR further enables the fabrication of core–shell structures, as demonstrated by ultrasound-assisted synthesis of ZnO–poly(methyl methacrylate) (ZnO–PMMA) hybrid NPs (~90 nm).[175] A 4 wt% hybrid NP coating extends mild steel (MS) service life, increasing impedance to 2 m^2.

Segmented flow microchannel reactors produce monodisperse spherical lignin NPs (LNS) with high specific surface area and uniform size (~13 nm).[176] These LNS maintain size stability for 60 days and form smooth PVA composite films with enhanced thermal stability (50% weight loss at 388 °C) and 13.3% improved UV shielding (1 wt% LNS at 250 nm). RPBR enables the fabrication of ultrafine layered hexagonal Mg/Al-layered double hydroxide NPs (160 nm, Mg/Al = 3) with rounded edges.[177] These NPs enhance interfacial interactions with polypropylene, improving flame retardancy and thermal stability without compromising mechanical properties.

3.5 Application in the optical field

The regulatory effect of PI equipment on the optical properties of NMs is primarily reflected in three key aspects: optimizing the electronic structure through surface defect engineering, constructing efficient charge transport pathways to enhance electron–hole separation efficiency, and simultaneously suppressing the non-radiative recombination of photogenerated carriers. This multi-scale regulation enables precise tuning of photoluminescence intensity, redshift/blueshift of absorption spectra, and bandgap energy modulation, thereby significantly improving photoluminescence quantum yield while enhancing fluorescence intensity and photocatalytic efficiency. It is worth noting that NMs prepared through PI strategies can exhibit advanced intelligent optical response characteristics, including selective transmission/shielding effects at specific wavelengths and reversible fluorescence switching behaviors. These performance improvements provide substantial opportunities for novel NMs in functional coatings, high-resolution bioimaging, precise molecular diagnostics, targeted drug delivery systems, next-generation flexible optoelectronic displays, and high-efficiency perovskite solar cells.

Research indicates that increasing the flow rate within the helical-coil microreactors (HCMR) enhances the crystallinity of SnO_2 NPs, reduces variations in lattice parameters, and decreases the proportion of surface oxygen vacancies.[178] At a high flow rate of 1.0 ml min^{-1}, the synthesized SnO_2 NPs exhibit a pure tetragonal phase, with a long-range ordered structure, redshifted absorption edge, and reduced bandgap energy to 3.92 eV. These findings provide a foundation for

optimizing optoelectronic and photocatalytic materials *via* fluid dynamics regulation in continuous flow synthesis.

Moreover, reactors such as RPBR and HSR, which possess excellent mixing and fragmentation capabilities, demonstrate significant advantages in reducing particle aggregation and enhancing material and elemental dispersion. RPBR can produce monodisperse MgAl layered double hydroxide (MgAl-LDH) NPs with an average particle size of only 31 nm within an extremely short reaction time of 20 s, achieving a visible light transmittance of 77.4% at 555 nm.[179] Photocatalysts, green materials using solar energy for chemical reactions, have great commercial potential. However, most systems only absorb ultraviolet light (4% of the solar spectrum), limiting efficiency and applicability. Developing visible-light-driven photocatalysts is a core focus in research. HSR enables the synthesis of smaller, less aggregated ZnO NPs. Compared to traditional stirrers, the single-particle size and secondary particle size are reduced from 9.69 nm and 955 nm to 7.09 nm and 26.5 nm, respectively, while providing more active sites, thereby increasing the photocatalytic degradation rate of MB from 38.6% to 70.8%.[180] Additionally, the high shear force generates an overpressure field in a short period, allowing molecules to accumulate sufficient nucleation energy within an extremely brief timeframe (approximately 1.03 ms).[181] This avoids heterogeneous nucleation defects and facilitates the synthesis of $Sn_xZn_{1-x}O_{1+x}$ NPs with more uniform elemental distribution, more pronounced bandgap changes, and enhanced photocatalytic activity. Ultrasonic treatment's cavitation effect also generates high temperature and pressure, significantly reducing particle size and minimizing aggregation. The resulting heterojunction nanocomposite ($YbVO_4/CuWO_4$) exhibits paramagnetic properties, with a reduced bandgap of 2.67 eV, enhanced visible light absorption, and a MB degradation rate reaching up to 100%.[182]

Traditional fluorescent dyes rely on UV light to trigger switches; however, UV light is harmful to cells, and irreversible fluorescence responses cause background interference. In contrast, CJIR-assisted FNP physically encapsulates the fluorescent group and quencher into biocompatible block copolymers, effectively overcoming these limitations.[183] The fluorescence resonance energy transfer efficiency of the formed 4CzIPNDAE with reversible fluorescence switching properties is significantly increased to 74.47%.

Efforts continue to explore methods for chemically modifying and precisely controlling base substances using specific functional groups or heteroatoms to synthesize new functional materials.[184] MWR represent an important approach for heteroatom modification of semiconductor materials and rapid synthesis of nanostructures with photoelectric detection performance. Uniform Ag doping in PbS improves the photoelectric detection performance of the Ag:PbS colloid, achieving a responsivity of 0.70 A W^{-1} and an external quantum efficiency of 164%.[185] Spherical Ti_3C_2-MXene quantum dots (Ti_3C_2-MQDs) with excellent fluorescence stability achieve fluorescence quenching and recovery through fluorescence resonance energy transfer with curcumin and oxidation–reduction reactions involving ClO^-, enabling selective detection of curcumin and ClO^-.[186] Through the synergistic processes of copper dissolution, Cu^+ doping, diffusion, and the strong interaction between CuNWs and ZnS, one-dimensional nanowire core–shell structures with roughened surfaces were successfully synthesized *in situ*. In the CuNWs/ZnS hybrid material, the CuNWs core is encapsulated by a porous ZnS shell (Fig. 13).[187] Its absorption edge red-shifted to 500 nm, showing

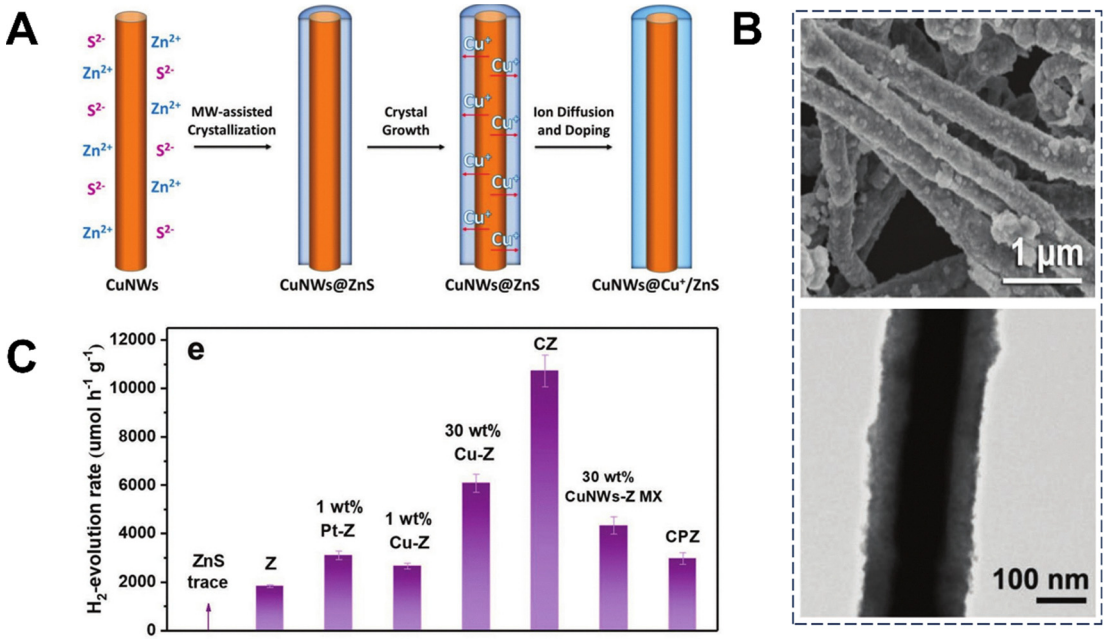

Fig. 13 (A) Schematic illustration of the CuNWs/ZnS hybrids formation by a microwave-assisted hydrothermal route. (B) FESEM (up) and TEM image of the as-prepared CuNWs/ZnS hybrids (CZ) (down). (C) Photocatalytic H_2 evolution rate of different samples under 420 nm LED light irradiation. Adapted with permission from ref. 187. Copyright 2019 Wiley-VCH.[187]

superior hydrogen production under 420 nm LED illumination with a rate of 10 722 μmol (h g)$^{-1}$ and quantum efficiency of 69%. Stability tests confirmed continuous operation for over 28 hours without significant performance loss.

3.6 Application in the electrochemical field

The particle size, dispersion state, interlayer spacing of crystals, crystal plane size, and uniformity of multi-metal co-deposition in NMs significantly influence their electrochemical properties, making these factors a focal point for electrochemical researchers. Introducing PI technology during preparation provides a feasible approach to achieve controllable regulation of these characteristics. Supercapacitors, with high power density, fast charging/discharging and long cycle life, are a key electrochemical energy storage technology. Nanosystems as electrode materials improve charge storage and transfer *via* high surface area and excellent conductivity, and are expected to further increase energy and power density. MCR has been widely applied to fabricate nanoelectrochemical materials with uniform small particle size, low aggregation, and high dispersion, such as Ni–MnO_2,[188] $BiFeO_3$,[189] Fe_3O_4,[190] and $KMnF_3$.[191] Supercapacitors prepared using these materials exhibit an energy density of 13.1 Wh kg^{-1} at a power density of 386.3 W kg^{-1}, with a capacitance retention rate of 81.2% after 5000 cycles. The integration of microfluidic and confined impinging flow technologies has demonstrated exceptional capability in the precise synthesis of layered composite materials, enabling the formation of porous nickel cobalt oxide (Ni–Co–O) composites and NiAl-LDH with controllable interlayer spacing.[192,193] The former exhibits superior ion diffusion and conductivity, with a

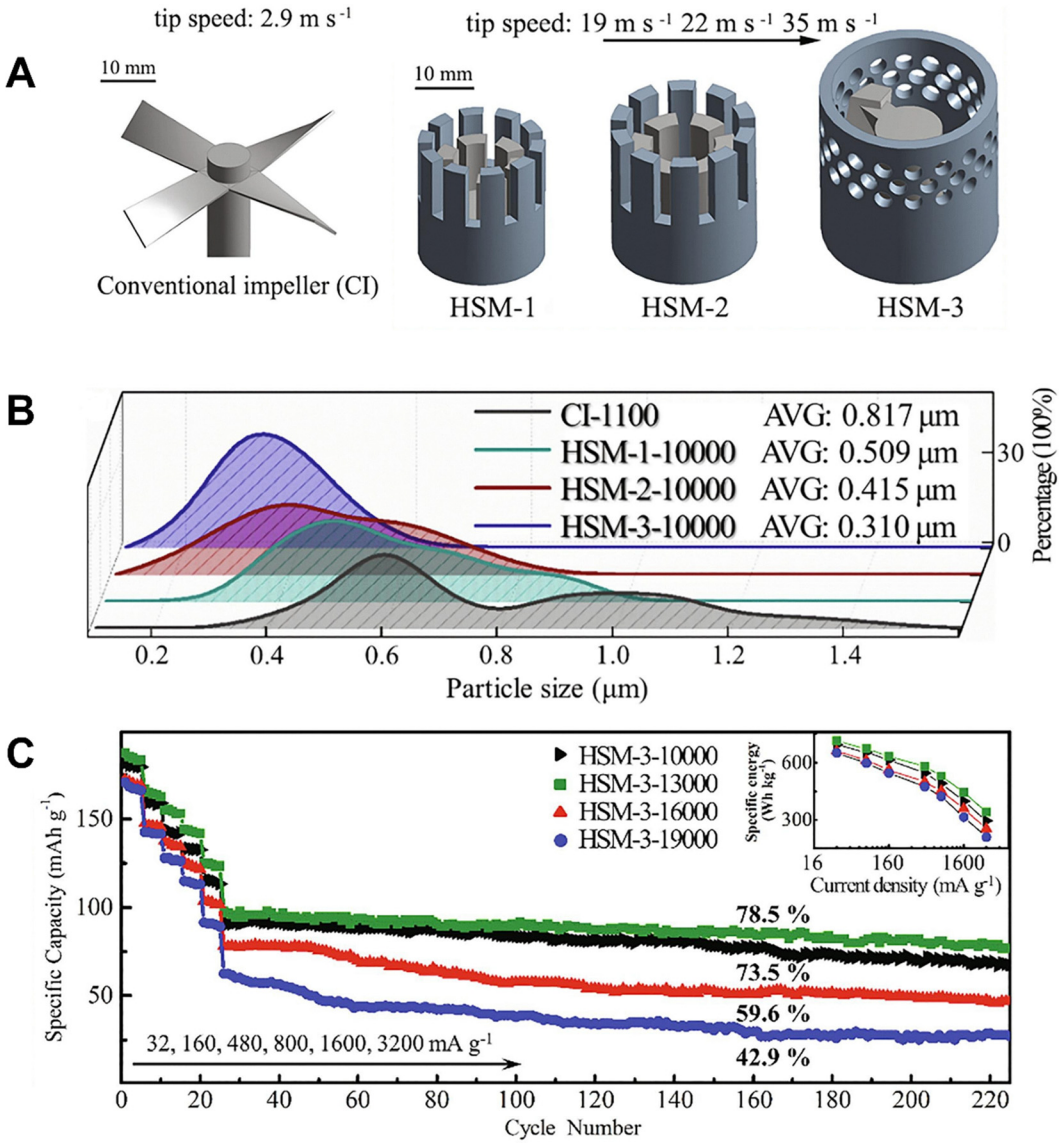

Fig. 14 (A) Conventional impeller (left), three HSM mixing heads with rotor–stator teethed (HSM-1, HSM-2), and blade-screen configuration (HSM-3) (right). (B) Particle size distribution of the synthesized samples. (C) Rate capabilities, specific discharge energies (inset) and cycling stabilities at various current densities. Adapted with permission from ref. 67. Copyright 2021 Elsevier.[67]

charge transfer resistance of only 0.2 Ω and specific capacitance of 2012 F g^{-1} at 1 A g^{-1}. After 2000 cycles at 5 A g^{-1}, it retains 93.9% of its initial capacity. The latter, LDH-20 with larger interlayer spacing, features a loose stacking, rough surface, irregular edge turbine-like layered mesoporous structure, and a high specific surface area of 48.9 m^2 g^{-1}, providing more reaction sites that enhance electrolyte penetration and promote Faraday reactions.

Lithium-ion batteries dominate high-energy-demand applications like portable devices and electric vehicles. To meet rising market demand, researchers are exploring higher-capacity cathode materials. Cobalt-free, nickel-rich layered oxides are attracting attention for their high energy density and sustainability. The exceptional micro-mixing performance and strong shear dispersion capability of HSR form the basis for its effectiveness in enhancing uniform multi-metal co-deposition. Through HSR and co-precipitation methods, layered $LiNi_{1/3}Co_{1/3}Mn_{1/3}O_2$ (Fig. 14) can be synthesized.[67] The optimal sample exhibits an average particle size of 236 nm, reduced charge transfer resistance, and improved Li^+ diffusion coefficient. After 200 cycles at 3200 mA g^{-1}, the material maintains a capacity of 98 mAh g^{-1} with cycle stability reaching 78.5%. This method is also applicable for preparing $LiNi_{0.60}Mn_{0.40}O_2$ and $LiNi_{0.60}Mn_{0.40-x}Fe_xO_2$ (NMFe, x = 0.01–0.05) NMs.[194] The latter achieves a discharge capacity of 185.3 mAh g^{-1} (0.1C, 2.8–4.5 V, 25 °C), surpassing the former's 182.5 mAh g^{-1}. Additionally, HSR enables the synthesis of La-intercalated $LiNi_{0.6}Co_{0.198}Mn_{0.2}La_{0.002}O_2$ NMs, which exhibit an initial dis-charge capacity of 200.5 mAh g^{-1}, outperforming materials without La.[195] This technique provides a promising tool for manufacturing heteroatom-inserted bulk nickel-rich cathode materials. Furthermore, SDR is employed to regulate lattice spacing. The resulting Prussian blue NPs display narrower diffraction peaks shifted toward smaller angles, larger lattice spacing, fewer lattice defects, and reduced crystalline water content.[196] When used as cathode materials in sodium-ion batteries, Prussian blue NPs enhance sodium content and maintain a capacity retention rate of 64.97% after 200 cycles at a current density of 170 mAh g^{-1}. SDR technology is also utilized to synthesize monodisperse spherical sulfur particles, reducing the average particle size to 82 nm and increasing the initial capacity to 1510 mAh g^{-1}.[197] In terms of *in situ* synthesis, UR offers irreplaceable advantages. Combining UR with spin-coating technology allows for the synthesis of single-crystal antimony sulfide iodide nanowires and antimony sulfide iodide–acrylonitrile composites on indium tin oxide substrates without high-temperature annealing.[198] The resulting photovoltaic devices, under 100 mW cm^{-2} white light illumination, achieve an average short-circuit current density of 1.84 μA cm^{-2} and an open-circuit voltage of 69 mV.

4. Conclusions

In summary, PI technology exhibits transformative potential in NM synthesis by reconstructing reaction environments through structural innovations (*e.g.*, microchannels), fluid-carrying energy (*e.g.*, impinging jets), and external field energy (*e.g.*, shear force, ultrasound, microwave, supergravity). This enables enhanced control over NM properties and functionality. The core regulatory mechanisms of PI are reflected in three dimensions: (1) by precisely modulating fluid dynamics, shear intensity, thermal gradients, and micro-mixing, PI enables fine-tuning of NM size, morphology, crystallinity, and dispersion. The spatial confinement and low shear characteristics of MCR and CIJR make them particularly suitable for gel preparation. The strong turbulence and high shear effects of RPBR, SDR, and HSR provide significant advantages in reducing particle size and improving dispersion. Moreover, the ultra-strong shear of HSR can promote directional crystallization and enhance the crystallinity of NMs. (2) PI technologies enable targeted surface modification, defect engineering, and interfacial control. MCR and CIJR optimize reaction kinetics *via* flow rate control, minimizing surface defects of NMs. MWR-assisted heteroatom doping (*e.g.*, nitrogen- or sulfur-modified carbon dots) enables bandgap structure regulation. UR-assisted self-assembly processes facilitate the formation of stable core–shell structures. (3) Comprehensive improvements in dispersion and stability are achieved through *in situ* synthesis techniques assisted by UR and MWR, as well as the synergistic strengthening of mechanical shear and high shear force fields in RPBR and HSR, effectively addressing agglomeration issues commonly encountered in traditional NM preparation. Furthermore, the synergistic enhancement of mixing and shearing in HSR improves the uniformity of multi-metal co-deposition.

5. Future prospects

Looking forward, to meet the demands for customized and intelligent synthesis of NMs, PI strategies will progressively evolve from single technologies toward multi-technology integration, intelligent control, green chemistry, and scalable deployment:

(1) Multi-technology coupling: integrating the narrow residence time distribution of MCR with the strong turbulence and high shear characteristics of HSR or RPBR, along with the directional induction and activation energy reduction effects of UR or MWR, to construct a segmented multi-field intensified reaction system, achieving simultaneous optimization of particle size, morphology, and surface defects in a single step.

(2) Computer-aided simulation: by integrating computational fluid dynamics with a population balance model that features a validated kernel, numerical simulations are conducted to systematically investigate the particle mixing dynamics within mixers, as well as the associated mechanisms of particle size evolution. Additionally, molecular dynamics simulations are employed to compute aggregation nuclei and elucidate atomic-scale phenomena.

(3) Intelligent-driven process: develop high-sensitivity tools with excellent spatiotemporal resolution to conduct *in situ* monitoring and real-time characterization of key parameters,

for rapid and accurate analyse particle formation process. Integrate the system with machine learning to create a multi-scale platform linking "equipment parameters – reaction kinetics – material properties". Finally, use artificial intelligence algorithms extract data from a wide range of datasets and adjust parameters dynamically, reducing optimization time and improving product performance.

(4) Green processes and application expansion: combining material synthesis methods (*e.g.*, template method, emulsion method, and gel method) with bio-derived solvents (*e.g.*, ionic liquids, deep eutectic solvents) and focusing on function-oriented NM design to develop environmentally friendly synthesis pathways.

(5) Scalability and materials innovation: deepening the understanding of dynamic mixing behavior within reactors, establishing reliable scale-up models. Developing novel low-cost, corrosion-resistant, and wear-resistant materials (*e.g.*, 3D-printed components, corrosion-resistant alloys, or ceramics) to reduce equipment manufacturing costs.

From MCRs to HSRs, PI strategies are propelling NM synthesis from empirical trial-and-error toward data-informed rational design. Through multi-tech synergy, intelligent platforms, and green process innovation, PI will become a cornerstone for bridging nanoscale discoveries and industrial-scale implementation, driving the next generation of advanced functional materials.

Author contributions

Z. X. F. investigation, visualization, writing – original draft. J. H. G. conceptualization, writing – original, funding acquisition. Y. C. W., J. Y. S., and H. W. S. visualization. H. J. L. writing – review & editing. J. L. Z. writing – review & editing, funding acquisition. J. J. X. W. supervision, funding acquisition, writing – review & editing.

Conflicts of interest

There are no conflicts to declare.

Data availability

No primary research results, software or code have been included and no new data were generated or analysed as part of this review.

Acknowledgements

This work was supported by the National Natural Science Foundation of China (22408236), Talent Development Foundation of Xinjiang (CZ002740, 2024ZD016), Science and technology planning system of Shihezi University (RCZK202425, KF202403), and CNPC Innovation Found (2024DQ02-0211).

References

1 U. Shanker, M. Rani and C. M. Hussain, *Green functionalized nanomaterials for environmental applications*, 2021, vol. 3, pp. 43–80.
2 B. Mekuye and B. Abera, *Nano Sel.*, 2023, **4**, 486–501.
3 M. G. Lines, *J. Alloys Compd.*, 2008, **449**, 242–245.
4 S. Singh, P. Thiyagarajan, K. Mohan Kant, D. Anita, S. Thirupathiah, N. Rama, B. Tiwari, M. Kottaisamy and M. S. Ramachandra Rao, *J. Phys. D: Appl. Phys.*, 2007, **40**, 6312–6327.
5 L. Liu, M. Zhao, X. Pei, S. Liu, S. Luo, M. Yan, R. Shao, Y. Sun, W. Xu and Z. Xu, *Prog. Org. Coat.*, 2023, **179**, 107522.
6 W. Cheng and J. Wen, *Coord. Chem. Rev.*, 2022, **473**, 214825.
7 S. Ngasotter, K. A. M. Xavier, M. M. Meitei, D. Waikhom, Madhulika, J. Pathak and S. K. Singh, *Carbohydr. Polym. Technol. Appl.*, 2023, **6**, 100349.
8 J. Zhang, J. F. Lovell, J. Shi and Y. Zhang, *BMEMat*, 2025, **3**, e12080.
9 X. Zhu, J. Lei, C. Jiang, Z. Fang, W. Zhang, Z. Yang, R. Guo, R. Xu and X. Hu, *Mater. Today Bio*, 2025, **32**, 101668.
10 D. Zhang, T. Liu, J. Cheng, S. Liang, J. Chai, X. Yang, H. Wang, G. Zheng and M. Cao, *Ceram. Int.*, 2019, **45**, 12443–12448.
11 Z. Shariatinia and Z. Zolfaghari-Isavandi, *Optik*, 2020, **212**, 164682.
12 A. A. Keller, A. Ehrens, Y. Zheng and B. Nowack, *Nat. Nanotechnol.*, 2023, **18**, 834–837.
13 M. M. El-Kady, I. Ansari, C. Arora, N. Rai, S. Soni, D. K. Verma, P. Singh and A. E. D. Mahmoud, *J. Mol. Liq.*, 2023, **370**, 121046.
14 Y. Lu and S. Ozcan, *Nano Today*, 2015, **10**, 417–420.
15 V. R. Regatte and N. S. Kaisare, *Chem. Eng. Sci.*, 2011, **66**, 1123–1131.
16 G. J. Harmsen, *Chem. Eng. Process.*, 2007, **46**, 774–780.
17 N. Kockmann, M. Gottsponer and D. M. Roberge, *Chem. Eng. J.*, 2011, **167**, 718–726.
18 J. Tao, S. F. Chow and Y. Zheng, *Acta Pharm. Sin. B*, 2019, **9**, 4–18.
19 X. Zhang, Y. Wu, Z. Chen, J. Zhang, J. Chen, Y. Wang and J. Xu, *Chem. Eng. Sci.*, 2023, **280**, 118969.
20 C.-Y. Lee, W.-T. Wang, C.-C. Liu and L.-M. Fu, *Chem. Eng. J.*, 2016, **288**, 146–160.
21 S. Asano, S. Kudo and J.-i Hayashi, *Chem. Eng. J.*, 2024, **489**, 151183.
22 X.-h Ge, X.-l Huang, S.-z Huang, H.-f Zhang, X.-d Wang, C.-s Ye, T. Qiu and K. Xu, *Chem. Eng. Sci.*, 2022, **259**, 117845.
23 G. Xin, W. Zhu, Y. Deng, J. Cheng, L. T. Zhang, A. J. Chung, S. De and J. Lian, *Nat. Nanotechnol.*, 2019, **14**, 168–175.
24 Y. Xu, M. Zhang, H. Zhong, S. Xie, X. Zhu, H. Zhang, J. Wang and Y. Yang, *Chem. Eng. J.*, 2025, **504**, 158798.
25 Y. Ding, Q. Cheng, J. Lyu, Z. Liu, R. Yuan, F. Ma and X. Zhang, *Adv. Mater.*, 2024, **36**, 2400101.
26 V. S. Cabeza, *Adv. Microfluid.: New Appl. Biol., Energy, Mater. Sci.*, 2016, **17**, 385–410.

27 F. Guo, D. Guo, W. Zhang, Q. Yan, Y. Yang, W. Hong and G. Yang, *Eur. J. Pharm. Sci.*, 2017, **99**, 328–336.
28 M. Erfan, M. Gnambodoe-Capochichi, Y. M. Sabry, D. Khalil, Y. Leprince-Wang and T. Bourouina, *Adv. Mater. Interfaces*, 2025, **12**, 2400827.
29 T. W. Phillips, I. G. Lignos, R. M. Maceiczyk, A. J. DeMello and J. C. DeMello, *Lab Chip*, 2014, **14**, 3172–3180.
30 H. Huang, H. du Toit, S. Ben-Jaber, G. Wu, L. Panariello, N. T. K. Thanh, I. P. Parkin and A. Gavriilidis, *React. Chem. Eng.*, 2019, **4**, 884–890.
31 A. Bakhtiari and C. J. Kähler, *Biomicrofluidics*, 2024, **18**, 044101.
32 Y. Han, H. Li, T. Fu, D. Liu and X. Wang, *Chem. Eng. Sci.*, 2023, **275**, 118743.
33 A. Koshy, S. Ray and G. Das, *Chem. Eng. Sci.*, 2024, **295**, 120169.
34 H. Yuan, Y. Pan, J. Tian, Y. Chao, J. Li and H. C. Shum, *Sens. Actuators, B*, 2019, **298**, 126766.
35 S. Senkan, *Angew. Chem., Int. Ed.*, 2001, **40**, 2550–2551.
36 C. Li, H. Zhang, W. Liu, L. Sheng, M.-J. Cheng, B. Xu, G. Luo and Q. Lu, *Nat. Commun.*, 2024, **15**, 884.
37 P. Lemke, L. Schneider, W. Kunz, A. L. Rieck, P. S. Jäger, A. Bruckmann, B. Nestler, K. S. Rabe and C. M. Niemeyer, *Adv. Funct. Mater.*, 2024, **34**, 2313944.
38 K. Adavi and A. M. Dehkordi, *Chem. Eng. Process.*, 2021, **159**, 108239.
39 E. Madadi-Kandjani, A. Passalacqua and R. Fox, *Chem. Eng. Sci.*, 2023, **273**, 118634.
40 M. S. C. A. Brito, L. P. Esteves, C. P. Fonte, M. M. Dias, J. C. B. Lopes and R. J. Santos, *Chem. Eng. Res. Des.*, 2018, **134**, 392–404.
41 M. Icardi, E. Gavi, D. L. Marchisio, M. G. Olsen, R. O. Fox and D. Lakehal, *Appl. Math. Model.*, 2011, **35**, 1591–1602.
42 Z. Liu, L. Guo, T. Huang, L. Wen and J. Chen, *Chem. Eng. Sci.*, 2014, **119**, 124–133.
43 A. Nie, Z. Gao, L. Xue, Z. Cai, G. M. Evans and A. Eaglesham, *Chem. Eng. Sci.*, 2018, **184**, 14–24.
44 S. Pal, K. Madane and A. A. Kulkarni, *Chem. Eng. J.*, 2019, **369**, 1161–1171.
45 Y. Hao, J.-H. Seo, Y. Hu, H.-Q. Mao and R. Mittal, *AIP Adv.*, 2020, **10**, 045105.
46 Z. Gao, J. Han, Y. Bao and Z. Li, *Chin. J. Chem. Eng.*, 2015, **23**, 350–355.
47 C. P. Fonte, M. A. Sultan, R. J. Santos, M. M. Dias and J. C. B. Lopes, *Chem. Eng. J.*, 2015, **260**, 316–330.
48 D. V. R. Kumar, B. L. V. Prasad and A. A. Kulkarni, *Ind. Eng. Chem. Res.*, 2013, **52**, 17376–17382.
49 M. S. Khan, T. R. Shaikh, S. P. Kulkarni, A. A. Patil and A. A. Kulkarni, *Org. Process Res. Dev.*, 2025, **29**, 479–489.
50 L. Sang, Y. Luo, G.-W. Chu, J.-P. Zhang, Y. Xiang and J.-F. Chen, *Chem. Eng. Sci.*, 2017, **158**, 429–438.
51 M. Chang, Y. Wei, D. Liu, J. X. Wang and J. F. Chen, *Angew. Chem., Int. Ed.*, 2021, **60**, 26390–26396.
52 Z. Bao, K. Li, S. Wang, K. Gao, D. Zhang and M. Li, *Adv. Powder Technol.*, 2021, **32**, 1611–1618.
53 K. Yang, G. Chu, H. Zou, B. Sun, L. Shao and J.-F. Chen, *Chem. Eng. J.*, 2011, **168**, 1377–1382.
54 J. Chen and L. Shao, *China Particuol.*, 2003, **1**, 64–69.
55 X. Shi, Y. Xiang, L.-X. Wen and J.-F. Chen, *Chem. Eng. J.*, 2013, **228**, 1040–1049.
56 W. Li, J. Yan, Z. Yan, Y. Song, W. Jiao, G. Qi and Y. Liu, *Appl. Therm. Eng.*, 2018, **142**, 760–766.
57 W. Jiao, X. Wei, S. Shao and Y. Liu, *Chin. J. Chem. Eng.*, 2022, **45**, 133–142.
58 Z. Zhao, Y. Liu, X. Yu, C. Wang, B. Li, Y. Liu and W. Jiao, *Chem. Eng. Sci.*, 2025, **305**, 121120.
59 H.-J. Yang, G.-W. Chu, J.-W. Zhang, Z.-G. Shen and J.-F. Chen, *Ind. Eng. Chem. Res.*, 2005, **44**, 7730–7737.
60 Y.-C. Yang, Y. Xiang, C. Pan, H.-K. Zou, G.-W. Chu, M. Arowo and J.-F. Chen, *J. Chem. Eng. Jpn.*, 2015, **48**, 72–79.
61 J.-F. Chen, Y.-H. Wang, F. Guo, X.-M. Wang and C. Zheng, *Ind. Eng. Chem. Res.*, 2000, **39**, 948–954.
62 Y.-Y. Kuang, Z.-B. Zhang, M.-L. Xie, J.-X. Wang, Y. Le and J.-F. Chen, *Ind. Eng. Chem. Res.*, 2015, **54**, 8157–8165.
63 C.-C. Lin and Y.-C. Lin, *Ceram. Int.*, 2016, **42**, 17295–17302.
64 L. Agarwal, V. Pavani, D. P. Rao and N. Kaistha, *Ind. Eng. Chem. Res.*, 2010, **49**, 10046–10058.
65 W. Wang, H.-K. Zou, G.-W. Chu, Z. Weng and J.-F. Chen, *Chem. Eng. J.*, 2014, **240**, 503–508.
66 N. Tang, J. Wu, J. Guo, Y. Wang, H. Li, J. Wu and J. Zhang, *Ind. Eng. Chem. Res.*, 2025, **64**, 7189–7199.
67 Y. Song, M. Wang, J. Li, H. Cui, H. Su and Y. Liu, *Chem. Eng. J.*, 2021, **419**, 129281.
68 C. Yang, J. Zhang, W. Li, S. Shang and C. Guo, *Cryst. Res. Technol.*, 2017, **52**, 1700002.
69 S. Carrillo De Hert and T. L. Rodgers, *Chem. Eng. Sci.*, 2017, **167**, 265–277.
70 M. Gallassi, G. F. N. Gonçalves, T. C. Botti, M. J. B. Moura, J. N. E. Carneiro and M. S. Carvalho, *Chem. Eng. Sci.*, 2019, **204**, 270–286.
71 S. Hall, M. Cooke, A. El-Hamouz and A. J. Kowalski, *Chem. Eng. Sci.*, 2011, **66**, 2068–2079.
72 L. Yang, W. Li, J. Guo, W. Li, B. Wang, M. Zhang and J. Zhang, *Front. Chem. Sci. Eng.*, 2020, **15**, 384–398.
73 J. Gu, Q. Xu, H. Zhou, W. Li and J. Zhang, *Chem. Eng. Process.*, 2016, **101**, 16–24.
74 Y. Liu, Y. Zhang, J. Guo, W. Li, M. Zhou and J. Zhang, *Chem. Eng. J.*, 2023, **451**, 138567.
75 A. W. Pacek, P. Ding and A. T. Utomo, *Powder Technol.*, 2007, **173**, 203–210.
76 Y. Liu, J. Guo, W. Li, X. Yang, W. Li, M. Zhou and J. Zhang, *Chem. Eng. J.*, 2022, **429**, 132420.
77 J. Guo, Y. Liu, S. Zhao, H. Li, W. Li, J. Xia, J. Wu and J. Zhang, *Chem. Eng. J.*, 2023, **452**, 139235.
78 J. Guo, Y. Liu, G. Shan, H. Li, W. Li, H. Qin, J. Xia, J. Wu and J. Zhang, *Chem. Eng. Sci.*, 2023, **272**, 118605.
79 M. Jasińska, J. Bałdyga, M. Cooke and A. Kowalski, *Appl. Therm. Eng.*, 2013, **57**, 172–179.
80 J. R. Bourne and M. Studer, *Chem. Eng. Process.*, 1992, **31**, 285–296.
81 R. Zeferino-Díaz, J. C. Hilario-Martínez, M. Sánchez-Cantú, M. A. Fernández-Herrera and J. Sandoval-Ramirez, *Green Chem.*, 2019, **21**, 1417–1420.

82 J. Zhang, S. Xu and W. Li, *Chem. Eng. Process.*, 2012, **57–58**, 25–41.
83 V. Vashisth, K. Nigam and V. Kumar, *Chem. Eng. Sci.*, 2021, **232**, 116296.
84 J. Wu, J. Guo, Y. Liu, K. Ma, Y. Wang, W. Li, Y. Han, R. Chi, B. Long and J. Zhang, *Chem. Eng. J.*, 2025, **504**, 158812.
85 S. Xu, J. Shi, Q. Cheng, W. Li and J. Zhang, *Chem. Eng. Sci.*, 2013, **87**, 111–121.
86 S. D. Pask, O. Nuyken and Z. Cai, *Polym. Chem.*, 2012, **3**, 2698–2707.
87 N. C. Jacobsen and O. Hinrichsen, *Ind. Eng. Chem. Res.*, 2012, **51**, 11643–11652.
88 D. Wang, C. Gu, C. Sun, X. Ling, H. Peng, X. Yang, F. Yuan, J. Du and W. Yu, *Chem. Eng. J.*, 2023, **451**, 138790.
89 S. Fallahizadeh, M. Gholami, M. R. Rahimi, H. R. Rajabi, S. Djalalinia, A. Esrafili, M. Farzadkia and M. Kermani, *Heliyon*, 2024, **10**, e32440.
90 A. Aoune and C. Ramshaw, *Int. J. Heat Mass Transfer*, 1999, **42**, 2543–2556.
91 X.-S. Wu, Y. Luo, G.-W. Chu, Y.-C. Xu, L. Sang, B.-C. Sun and J.-F. Chen, *Ind. Eng. Chem. Res.*, 2018, **57**, 7692–7699.
92 K. Nomura and P. Terwilliger, *Spec. Matrices*, 2019, **7** 1–19.
93 L.-B. Yao, W. Wu, X.-S. Wu, G.-W. Chu, Y. Luo and B.-C. Sun, *Chem. Eng. Process.*, 2021, **166**, 108500.
94 K. V. K. Boodhoo and S. R. Al-Hengari, *Chem. Eng. Technol.*, 2012, **35**, 1229–1237.
95 A. Chianese, A. Picano and M. Stoller, *Chem. Eng. Trans.*, 2021, **84**, 121–126.
96 S. Mohammadi, A. Harvey and K. V. K. Boodhoo, *Chem. Eng. J.*, 2014, **258**, 171–184.
97 H.-S. Liu, Y.-H. Wang, C.-C. Li and C. Y. Tai, *Chem. Eng. J.*, 2012, **183**, 466–472.
98 M. Hassellöv, J. W. Readman, J. F. Ranville and K. Tiede, *Ecotoxicology*, 2008, **17**, 344–361.
99 K. Boodhoo, *Process Intensif. Green Chem.*, 2013, 59–90.
100 W. H. Khan and V. K. Rathod, *Chem. Eng. Process.*, 2014, **80**, 1–10.
101 B. de Caprariis, M. Di Rita, M. Stoller, N. Verdone and A. Chianese, *Chem. Eng. Sci.*, 2012, **76**, 73–80.
102 M.-H. Chang, H.-S. Liu and C. Y. Tai, *Powder Technol.*, 2011, **207**, 378–386.
103 A. Gedanken, *Ultrason. Sonochem.*, 2004, **11**, 47–55.
104 P. A. Tatake and A. B. Pandit, *Chem. Eng. Sci.*, 2002, **57**, 4987–4995.
105 R. Mettin, C. Cairós and A. Troia, *Ultrason. Sonochem.*, 2015, **25**, 24–30.
106 B. A. Bhanvase, N. S. Darda, N. C. Veerkar, A. S. Shende, S. R. Satpute and S. H. Sonawane, *Ultrason. Sonochem.*, 2015, **24**, 87–97.
107 S. Cui, S. Zhang, S. Ge, L. Xiong and Q. Sun, *Ind. Crops Prod.*, 2016, **83**, 346–352.
108 H. Kalawoun, C. Ciotonea, M. Marinova, C. Gennequin and F. Delattre, *Ultrason. Sonochem.*, 2024, **104**, 106806.
109 X. Gao, A. I. Isayev, X. Zhang and J. Zhong, *Compos. Sci. Technol.*, 2017, **144**, 125–138.
110 K. S. Suslick and D. J. Flannigan, *Annu. Rev. Phys. Chem.*, 2008, **59**, 659–683.
111 K. S. Suslick, S. Doktycz and E. Flint, *Ultrasonics*, 1990, **28**, 280–290.
112 Y.-q Gao, N.-y Gao, W. Wang, S.-f Kang, J.-h Xu, H.-m Xiang and D.-q Yin, *Ultrason. Sonochem.*, 2018, **49**, 33–40.
113 K. S. Suslick and G. J. Price, *Annu. Rev. Mater. Res.*, 1999, **29**, 295–326.
114 G. Guo, Y. Ma, Y. Guo, C. Zhang, X. Guo, J. Tu, A. C. Yu, J. Wu and D. Zhang, *Ultrason. Sonochem.*, 2017, **37**, 279–285.
115 X. Li, C. Pu, X. Chen, F. Huang and H. Zheng, *Ultrason. Sonochem.*, 2021, **70**, 105291.
116 K. Büyükkanber, A. Ekinci and Ö. Şahin, *Int. J. Hydrogen Energy*, 2024, **79**, 335–345.
117 Z. Wei, X. Bai, A. Maximov and W. Wu, *Ultrason. Sonochem.*, 2024, **103**, 106793.
118 Z. Dong, D. Fernandez Rivas and S. Kuhn, *Lab Chip*, 2019, **19**, 316–327.
119 T. Hosseini, M. Haghighi and H. Ajamein, *Energy Convers. Manage.*, 2016, **126**, 595–607.
120 S.-t Deng, H. Yu, D. Liu and Y.-g Bi, *Appl. Phys. A: Mater. Sci. Process.*, 2017, **123**, 105291.
121 P. Adamou, E. Harkou, A. Villa, A. Constantinou and N. Dimitratos, *Ultrason. Sonochem.*, 2024, **107**, 106925.
122 B. Ashley, P. N. Vakil, B. B. Lynch, C. M. Dyer, J. B. Tracy, J. Owens and G. F. Strouse, *ACS Nano*, 2017, **11**, 9957–9967.
123 C. Xu, J. Lan, J. Ye, Y. Yang, K. Huang and H. Zhu, *Chem. Eng. J.*, 2023, **452**, 139690.
124 Z. Li, K. Peng, N. Ji, W. Zhang, W. Tian and Z. Gao, *Nanoscale Adv.*, 2025, **7**, 419–432.
125 C. O. Kappe, A. Stadler and D. Dallinger, *Microwaves in organic and medicinal chemistry*, 2012, vol. 3, pp. 41–81.
126 R. Hayakawa and Y. Takano, *Thin Solid Films*, 2017, **636**, 171–176.
127 J. Jouhannaud, J. Rossignol and D. Stuerga, *J. Solid State Chem.*, 2008, **181**, 1439–1444.
128 Y. Zhao, B. Liu, L. Zhang and S. Guo, *J. Hazard. Mater.*, 2020, **396**, 122740.
129 R. Manno, V. Sebastian, R. Mallada and J. Santamaria, *Ind. Eng. Chem. Res.*, 2019, **58**, 12702–12711.
130 L. Panariello, M. O. Besenhard, S. Damilos, A. Sergides, V. Sebastian, S. Irusta, J. Tang, N. T. K. Thanh and A. Gavriilidis, *Chem. Eng. Process.*, 2022, **182**, 109198.
131 Y. Lin, D. W. Baggett, J.-W. Kim, E. J. Siochi and J. W. Connell, *ACS Appl. Mater. Interfaces*, 2011, **3**, 1652–1664.
132 R. C. Seyfeli and D. Varisli, *Int. J. Hydrogen Energy*, 2022, **47**, 15175–15188.
133 S. H. Jhung, J.-S. Chang, J. S. Hwang and S.-E. Park, *Microporous Mesoporous Mater.*, 2003, **64**, 33–39.
134 A. V. Nikam and A. H. Dadwal, *Adv. Powder Technol.*, 2019, **30**, 13–17.
135 A. Pein, M. Baghbanzadeh, T. Rath, W. Haas, E. Maier, H. Amenitsch, F. Hofer, C. O. Kappe and G. Trimmel, *Inorg. Chem.*, 2010, **50**, 193–200.

136 M. Miyakawa, N. Hiyoshi, H. Koda, K. Watanabe, H. Kunigami, H. Kunigami, A. Miyazawa and M. Nishioka, *RSC Adv.*, 2020, **10**, 6571–6575.
137 F. Cameli, C. Xiouras and G. D. Stefanidis, *CrystEngComm*, 2018, **20**, 2897–2901.
138 S. Ngasotter, K. A. M. Xavier, L. Porayil, A. K. Balange, B. B. Nayak and G. Ninan, *ACS Sustainable Chem. Eng.*, 2024, **12**, 17222–17235.
139 M. K. Bayazit, J. Yue, E. Cao, A. Gavriilidis and J. Tang, *ACS Sustainable Chem. Eng.*, 2016, **4**, 6435–6442.
140 C.-Y. Ma, X. Gao, X.-P. Peng, Y.-F. Gao, J. Liu, J.-L. Wen and T.-Q. Yuan, *Ind. Crops Prod.*, 2021, **164**, 113415.
141 Z. Zhu, K. Yao, J. Gao, Q. Liu, J. Feng, C. Chen and L. Ye, *Chem. Eng. Sci.*, 2025, **304**, 120972.
142 M. Kather, F. Ritter and A. Pich, *Chem. Eng. J.*, 2018, **344**, 375–379.
143 F. Kang, D. Wang, Y. Pu, X.-F. Zeng, J.-X. Wang and J.-F. Chen, *Powder Technol.*, 2018, **325**, 405–411.
144 Z. Zhang and J. Ji, *Powder Technol.*, 2017, **305**, 546–552.
145 W. R. Rathod and V. K. Rathod, *J. Chem. Technol. Biotechnol.*, 2018, **94**, 919–926.
146 H. Chen, B. Xu, C. Zhou, A. E.-G. A. Yagoub, Z. Cai and X. Yu, *Food Hydrocolloids*, 2022, **122**, 107110.
147 Z. Liu, M. Yang, W. Yao, T. Wang and G. Chen, *Chem. Eng. Sci.*, 2023, **280**, 119052.
148 N. Matman, Y. Min Oo, T. Amnuaikit and K. Somnuk, *Ultrason. Sonochem.*, 2022, **83**, 105926.
149 Q. Chen, K. Chen, F. Yu, A. Guo, S. Zou, M. Zhou, J. Li, J. Dan, Y. Li, B. Dai and X. Guo, *Ind. Eng. Chem. Res.*, 2022, **61**, 9300–9310.
150 Y. Guo, Y. Wei, M. Chang, D. Wang, J. X. Wang and J. F. Chen, *AIChE J.*, 2023, **69**, e18181.
151 W. Jiao, Y. Song, D. Zhang, G. Chang, H. Fan and Y. Liu, *Adv. Powder Technol.*, 2019, **30**, 2251–2261.
152 Y. Song, Z. Li, S. Shao, W. Jiao and Y. Liu, *Adv. Powder Technol.*, 2021, **32**, 1584–1593.
153 J. López-Tinoco, J. Lara-Romero, R. Rangel, J. Apolinar-Cortés, F. Paraguay-Delgado, S. Jiménez-Sandoval, L. Bazán-Díaz and R. Mendoza-Cruz, *J. Mater. Res. Technol.*, 2021, **13**, 70–82.
154 Q. Chen, X. Xue, Y. Liu, A. Guo, K. Chen, J. Yin, F. Yu, H. Zhu and X. Guo, *J. Hazard. Mater.*, 2022, **438**, 129524.
155 A. Dastbaz, J. Karimi-Sabet and M. A. Moosavian, *Chem. Eng. Process.*, 2019, **135**, 245–257.
156 G. Sargazi, D. Afzali and A. Mostafavi, *Appl. Organomet. Chem.*, 2019, **33**, e4816.
157 H. Xiao, Y. Song, J. Chen, H. Ma, L. Wang, Y. Xiang and L. Shao, *Chemosphere*, 2023, **340**, 139848.
158 S. Shao, Z. Li, K. Gao, J. Zhang, Y. Liu and W. Jiao, *Sep. Purif. Technol.*, 2022, **280**, 119896.
159 H. R. Mahmoud, S. A. El-Molla and M. A. Naghmash, *Ultrasonics*, 2019, **95**, 95–103.
160 Z. Fu, Y. Bao, Y. Zhang, Z. Yang, L. Zhou, L. Li, S. Dai, X. Hu and X. Guo, *Sep. Purif. Technol.*, 2024, **351**, 128008.
161 Y. Li, S. Wang, Q. Wang, M. Zhu, W. Shan and Y. Liu, *Catal. Sci. Technol.*, 2023, **13**, 1874–1887.
162 V. Nicolosi, M. Chhowalla, M. G. Kanatzidis, M. S. Strano and J. N. Coleman, *Science*, 2013, **340**, 6139.
163 X. Zhou, J. Dan, J. Zhang, S. Yang, L. Shi, J. Wang, B. Dai, F. Yu and J. Zhang, *Chem. Eng. Process.*, 2019, **145**, 107664.
164 M. Ahmadi Khoshooei, C. E. Scott, L. Carbognani and P. Pereira-Almao, *Catal. Today*, 2021, **365**, 132–141.
165 J. Prekodravac, B. Vasiljević, Z. Marković, D. Jovanović, D. Kleut, Z. Špitalský, M. Mičušik, M. Danko, D. Bajuk–Bogdanović and B. Todorović–Marković, *Ceram. Int.*, 2019, **45**, 17006–17013.
166 A. Adamu, F. Russo Abegão and K. Boodhoo, *Tetrahedron Green Chem.*, 2023, **1**, 100007.
167 L. Iezzi, G. Vilardi, G. Saviano and M. Stoller, *Chem. Eng. J.*, 2022, **449**, 137864.
168 S. J. Skosana, C. Khoathane and T. Malwela, *Polym. Bull.*, 2020, **78**, 203–221.
169 T. Harifi and M. Montazer, *Ultrason. Sonochem.*, 2015, **27**, 543–551.
170 F. S. Ghaheh, A. Khoddami, F. Alihosseini, S. Jing, A. Ribeiro, A. Cavaco-Paulo and C. Silva, *Process Biochem.*, 2017, **59**, 46–51.
171 J. Kwiczak-Yiğitbaşı, M. Demir, R. E. Ahan, S. Canlı, U. Ö. Ş afak Şeker and B. Baytekin, *ACS Sustainable Chem. Eng.*, 2020, **8**, 18879–18888.
172 H. Barani and B. Mahltig, *Cellulose*, 2020, **27**, 9105–9121.
173 K. H. Le, M. D.-B. Nguyen, L. D. Tran, H. P. Nguyen Thi, C. V. Tran, K. V. Tran, H. P. Nguyen Thi, N. Dinh Thi, Y. S. Yoon, D. D. Nguyen and D. D. La, *Prog. Org. Coat.*, 2021, **158**, 106339.
174 B. Xue, T. Sun, J.-k Wu, F. Mao and W. Yang, *Ultrason. Sonochem.*, 2015, **22**, 1–6.
175 S. B. Potdar, B. V. S. Praveen and S. H. Sonawane, *Ultrason. Sonochem.*, 2020, **68**, 105200.
176 T. Ju, Z. Zhang, Y. Li, X. Miao and J. Ji, *RSC Adv.*, 2019, **9**, 24915–24921.
177 H.-Y. Zeng, P.-H. Zhu, S. Xu, M.-C. Liao, Z.-Q. Zhang, X.-J. Liu and J.-Z. Du, *Ind. Eng. Chem. Res.*, 2014, **53**, 18380–18389.
178 M. Periyasamy, S. K. Saha, V. Balamurugan, U. Sengupta, S. Sain, C. Pichandi, M. Sudharsan Natteri and A. Kar, *J. Ind. Eng. Chem.*, 2025, DOI: **10.1016/j.jiec.2025.03.052**.
179 B. Chen, Q. Sun, D. Wang, X.-F. Zeng, J.-X. Wang and J.-F. Chen, *Ind. Eng. Chem. Res.*, 2020, **59**, 2960–2967.
180 Z. Zeng, X. Tian, Y. Qian, Z. Wang, J. Liao, P. Li and X. Zhang, *Powder Technol.*, 2024, **433**, 119218.
181 Z. Zeng, X. Tian, H. Cheng, X. Zhao, L. Qiu, J. Liao, P. Li and X. Zhang, *J. Alloys Compd.*, 2024, **1003**, 175611.
182 M. Eghbali-Arani, A. Sobhani-Nasab, M. Rahimi-Nasrabadi, F. Ahmadi and S. Pourmasoud, *Ultrason. Sonochem.*, 2018, **43**, 120–135.
183 J. Liu, Y. Wu, J. Tang, T. Wang, F. Ni, Q. Wu, X. Yang, A. Ayyaz, N. Ramzan and Y. Xu, *Chin. J. Chem. Eng.*, 2023, **56**, 89–96.
184 M. Terrones, A. Jorio, M. Endo, A. M. Rao, Y. A. Kim, T. Hayashi, H. Terrones, J. C. Charlier, G. Dresselhaus and M. S. Dresselhaus, *Mater. Today*, 2004, **7**, 30–45.

185 M. Shkir, M. T. Khan, I. M. Ashraf, S. AlFaify, A. M. El-Toni, A. Aldalbahi, H. Ghaithan and A. Khan, *Ceram. Int.*, 2019, **45**, 21975–21985.
186 M. Liu, Y. Bai, Y. He, J. Zhou, Y. Ge, J. Zhou and G. Song, *Microchim. Acta*, 2021, **188**, 430062.
187 S. Xiao, W. Dai, X. Liu, D. Pan, H. Zou, G. Li, G. Zhang, C. Su, D. Zhang, W. Chen and H. Li, *Adv. Energy Mater.*, 2019, **9**, 1900775.
188 J. Zhang, L. Zhu, H. Jia, K. Wei and L. Wen, *J. Alloys Compd.*, 2021, **889**, 161772.
189 R. S. Abiev, O. V. Almjasheva, V. I. Popkov and O. V. Proskurina, *Chem. Eng. Res. Des.*, 2022, **178**, 73–94.
190 S. Wang, J. Zhang, K. Ma, W. Zhang, Y. Gao, P. Yu, S. Zhao, Y. Feng, J. Yang, R. Sun, Y. Li, N. Zhu, W. He and K. Guo, *Chem. Eng. J.*, 2024, **501**, 157672.
191 K.-P. Cheng, R.-J. Gu and L.-X. Wen, *RSC Adv.*, 2020, **10**, 11681–11693.
192 Q.-C. Zhang, L.-L. Tian, Y.-C. Wu, Y. Li, L.-X. Wen and S. Wang, *J. Alloys Compd.*, 2019, **792**, 314–327.
193 Z. Tan, X. Luo, T. Wei, F. Zhang, Y. Lv, L. Chen and Y. Shi, *Energy Fuels*, 2020, **34**, 8939–8946.
194 J. Liao, C. Wang, J. Liu, G. Shan, X. Huo, P. Sun, N. Nie, J. Zhang and W. Li, *Ind. Eng. Chem. Res.*, 2024, **63**, 11959–11970.
195 J. Liu, H. Zhang, G. Shan, M. Liu, J. Liao, Y. Zhao, P. Sun, J. Zhang, S. Zou, N. Nie and W. Li, *J. Alloys Compd.*, 2024, **991**, 174515.
196 P. Zhu, Y. Wang, J. Li and Y. Jin, *ACS Appl. Energy Mater.*, 2023, **6**, 6141–6150.
197 A. Dell'Era, F. A. Scaramuzzo, M. Stoller, C. Lupi, M. Rossi, D. Passeri and M. Pasquali, *Appl. Sci.*, 2019, **9**, 1913.
198 K. Mistewicz, W. Matysiak, M. Jesionek, P. Jarka, M. Kępińska, M. Nowak, T. Tański, D. Stróż, J. Szade, K. Balin and T. Rzychoń, *Appl. Surf. Sci.*, 2020, **517**, 146138.

